PHASE-SPACE DISSIMILARITY MEASURES OF NONLINEAR DYNAMICS: INDUSTRIAL AND BIOMEDICAL APPLICATIONS

V. Protopopescu* and L. M. Hively
Oak Ridge National Laboratory
Oak Ridge, TN 37831-6016, USA

Invited review paper in *Recent Research Developments in Physics* (2005)

Running title: Dissimilarity measures of nonlinear dynamics

* Corresponding author: vvp@ornl.gov; tel: 1-865-574-4722; fax: 1-865-574-0405

ABSTRACT

One of the most important problems in time-series analysis is the suitable characterization of the dynamics for timely, accurate, and robust condition assessment of the underlying system. Industrial applications involve prognostication of machine failures, thus reducing costly machine repairs, avoiding complete breakdown with potentially catastrophic effects, and decreasing concomitant and human down-time. Biomedical applications include detection and forewarning of abnormal physiological behavior to avoid (or at least reduce) the harmful effects of various medical crises, decrease patient hospitalization, and lower costs of health care and lost productive time.

Both machine and physiological processes display complex, non-stationary behaviors that are affected by noise and may range from (quasi-)periodic to completely irregular (chaotic) regimes. Nevertheless, extensive experimental evidence indicates that even when the systems behave very irregularly (e.g., severe tool chatter or cardiac fibrillation), one may assume that - for all practical purposes - the dynamics are confined to low dimensional manifolds. As a result, the behavior of these systems can be described via traditional nonlinear measures (TNM), such as Lyapunov exponents, Kolmogorov entropy, and correlation dimension. However, while these measures are adequate for discriminating between clear-cut regular and chaotic dynamics, they are not sufficiently sensitive to distinguish between slightly different irregular (chaotic) regimes, especially when data are noisy and/or limited. Both machine and physiological dynamics usually fall into this latter category, creating a massive stumbling block to prognostication of abnormal regimes.

We present here a recently developed approach that captures more efficiently changes in the underlying dynamics. We start with process-indicative, time-serial data, recognizing that some data capture most aspects of the dynamics, while other data may not. The data are checked for quality, and inadequate data (e.g., lost data points, intervals with unchanged signal amplitude, excessive periodic content, excessive noise, saturation at high or low limits, and inconsistent signal amplitude across datasets in a test sequence) are discarded. Acceptable data are filtered to remove confounding artifacts (e.g., sinusoidal variation in three-phase electrical signals or eye-blinks and muscular activity in EEG). The artifact-filtered data are then used to recover the essential features of the underlying dynamics via standard time-delay, phase-space reconstruction. One of the main results of this reconstruction is a discrete approximation of the distribution function (DF) on the attractor. Unaltered dynamics yield an unchanging geometry of the attractor and the visitation frequencies of its various points, corresponding to the baseline DF. Condition change is established by comparing the baseline DFs to subsequent test-case DFs via new, phase space dissimilarity measures (PSDM), namely the L_1 distance and χ^2 statistic between two DFs. A clear trend in the dissimilarity measures over time indicates substantial departure from the baseline dynamics, thus signaling condition change. The severity of this departure can be interpreted as a "normal" fluctuation, abnormal behavior, impending failure, or complete breakdown.

We illustrate the new approach on an assortment of machinery and biomedical examples. The machine data were collected from laboratory tests of various industrial equipment for diverse failure modes via seeded faults and accelerated failures. The biomedical applications involve detection of physiological changes, such as epileptic seizures from EEG; ventricular fibrillation fainting, and sepsis onset from ECG; and breathing difficulty from chest sounds. The PSDM show a consistent discrimination of normal-to-abnormal transitions, allowing earlier, more accurate, and more robust detection of the dynamical change for all of these applications in comparison to TNM.

I. INTRODUCTION

Response to an abnormal event (e.g., condition-based or predictive maintenance of machines, and treatment of a patient) relies heavily on analysis of noisy data. The major roadblocks to accurate, timely, and robust prognostication include [1]: (a) incomplete understanding of event evolution to the abnormal state; (b) lack of predictive methodologies for unsteady signatures; (c) ignorance about controlling parameters; and (d) unavailability of test facilities to emulate a real, operational industrial environment or inappropriateness of such tests in humans. Our present approach is far from proposing a complete and universally applicable solution to this problem, but does offer a partial solution. In particular, we address items (a)-(b) by quantifying the (non-stationary) condition change as a sequence of nonlinear statistical signatures; item (c) by associating change in the controlling parameter with the response of the equipment or biomedical process; and item (d) by tests that resemble in-plant operations or use of real physiological data for the biomedical endpoint.

Machine dynamics [2-27] has a long history [11]. Metal cutting forces during machine tool chatter have long been recognized as "very complex" and "very far from sinusoidal," implying nonlinear dynamics [23]. Tlusty[12, 18-20] published extensive experimental (in)stability diagrams for turning, milling, boring, hobbing, and planing. Qu *et al*. [16] used nonlinear measures to diagnose dynamics, using vibration data from rotating machinery (turbo-generator and compressor). Bukkapatnam et al. [3] analyzed data from lathe cutting and found low dimensional, chaotic features. Our previous work focused on the nonlinear dynamics of machine tool chatter [28, 29], and used phase-space (PS) dissimilarity to detect condition change in various physical processes, namely: distinguishing different drilling conditions (tool wear) from spindle motor current of a machining center; distinguishing (un)balanced centrifugal pump states from electrical motor power; and forewarning of a bellows coupling failure in a rotating drive train from motor current. [30] Our more recent work used phase-space dissimilarity to determine condition change in machines due to seeded faults and accelerated failure progression [31-33]. Delogu, Rustici, and coworkers found hyperchaos [34] and intermittent chaos [35] in ball milling. Pfeiffer's analysis [36] showed that bifurcations and chaos may be generated by various mechanical processes, such as stick-slip due to dynamic/static friction and surface impacts; additional processes include surface deformation and material removal/wear [12, 18, 20].

Characterization of change in physiological processes is even more vexing, displaying the same confounding features of non-stationarity, nonlinearity, multiple time scales, and strong sensitivity to environmental perturbations, with the added challenge of the enormous complexity of a living organism. As an illustration of the status of biomedical prognostics, we shall briefly describe recent work on prediction of epileptic events. Early work on prediction of epileptic seizures began in the 1970s [37], expanding rapidly over the last decade, due to digital electroencephalographic (EEG) technology and advances in nonlinear dynamics [38-44]. Babloyantz and Destexhe [45], and Babloyantz [46] suggested that EEG data have noisy deterministic features that produce diverse behaviors, including chaos, although some investigators have challenged this idea [47-49]. Recently, the *Journal of Clinical Neurophysiology* published a recent focus issue (May 2001) on epilepsy prediction [50-55]. Litt and Echauz [56] reviewed this research in May 2002, including time- and frequency-domain analysis, nonlinear dynamics and chaos, as well as neural networks and other artificial intelligence approaches. *IEEE Transactions on Biomedical Engineering* published a focus issue (May 2003) on prediction of epilepsy [57-68]. Typical measures for prediction include the largest Lyapunov exponent [61], synchrony [57], correlation integral [65], and various time- and frequency-domain features of EEG energy [58]. These results are mostly based on analysis of *intracranial* EEG.

To date, most of the effort on condition change assessment and forewarning has focused on Fourier spectra, conventional statistical measures (CSM), and traditional nonlinear measures (TNM), such as Kolmogorov entropy, correlation dimension, and Lyapunov exponents. While these descriptors discriminate adequately between clear-cut regular and chaotic dynamics, they are not always

sufficiently sensitive to distinguish between slightly different chaotic regimes, especially when data are limited and/or noisy. This lack of discrimination arises from averaging over the global dynamics, which erases most of the dynamical details. Indeed, our initial analysis of machine data [28] and EEG data [69] used TNM, yielding inconsistent detection and event forewarning. Those results indicated that detection of meaningful information in attenuated, noisy, artifact-infested signals requires more sensitive and discriminating measures.

We addressed these limitations by defining new measures to quantify change in time-serial data, which are converted to a discrete geometric (phase space) representation. A distribution function describes the visitation frequency and sequence of the discrete phase-space states; (un)changing dynamics lead to an (un)altered distribution function. Dissimilarity measures quantify change between test case and baseline DFs. Large dissimilarity means that the system is far from the baseline, as a forewarning of an abnormal, possibly catastrophic event. A comparison of the results shows a significant and consistent superiority of the new measures over the TNM for detection and forewarning of condition change in both machinery and physiological data. Indeed, the PSDM have consistently better sensitivity and discrimination power for event forewarning than TNM for machines [70] and biomedical data [71].

The remainder of this paper is organized as follows. In Section II we review briefly the traditional statistical and nonlinear measures used to characterize change in time serial data. We then present our methodology and the associated PSDM including a recently developed [32] statistical test for failure forewarning and onset. Section III and IV present our results for various machine and physiological data, respectively. Section V summaries the results and presents our conclusions.

II. APPROACH

Machine processes display rich dynamics, including quasi-periodicity, nonlinearity, and occasional chaos. To carry out the analysis, we assume that: (i) the underlying dynamics are essentially deterministic; (ii) the processes behave as a low-dimensional nonlinear, possibly chaotic dynamical system; (iii) a single channel of data can capture the main features of nonlinear dynamics. Phase-space reconstruction of multi-channel data is also possible. Preliminary results [72] support the assumption that multi-channel data provide more robust forewarning than single channel data. A thorough investigation of these aspects will be pursued in the future.

Several practical caveats are related to the amount of data and its quality. For example, an insufficient amount of time-serial data may not adequately sample the attractor, thereby degrading the sensitivity of the dissimilarity measures [73, 74]. Likewise, the data sampling rate, f_s, must be much larger than the machine dynamical rate, ν, which in turn must be much larger when compared to the inverse of the time, T, to failure: $f_s >> \nu >> 1/T$. We assure the validity of this assumption by requiring that the first minimum in the mutual information function occur at four (or more) time steps. Usually, the analysis is confounded by artifacts in the data. Based on *a priori* information about the underlying dynamics, we remove such artifacts (e.g., sinusoidal variation in three-phase electrical power, resonant oscillations in vibration power, low-frequency, muscular activity in physiological data from eye-blinks and breathing). Also, parameters for the phase-space reconstruction must be chosen carefully for robust and sensitive indication of condition change. This part of the methodology is still quite analyst-intensive; practical (analyst independent) prognostication must be less dependent on interaction with or guidance from the human expert. Moreover, the applicability of the present methodology has been limited to *retrospective* analysis of *archival* data for seeded faults, accelerated failures, and biomedical events which are well characterized under appropriate test conditions. The separation between the present state of our methodology and the real-world needs is still large and will require substantial additional development, since practical applications will definitely require *prospective* analysis of (*near-*)*real-time* data.

The general approach is outlined next. We first acquire a process-indicative scalar signal, e, which is sampled at equal time intervals, τ, starting at an initial time, t_0, yielding a time-serial sequence of N

points, $e_i = e(t_0 + i\tau)$. We remove artifacts from the data with a zero-phase quadratic filter [69, 75, 76] that performs better than conventional filters. This filter uses a moving window of $2w+1$ points of data, with the same number of data points, w, on either side of a central point. We fit a parabola in the least-squares sense to these data points, and use the central point of the fit to estimate the low-frequency artifact, f_i. The residual (artifact-filtered) signal, $g_i = e_i - f_i$, has essentially no low-frequency artifact activity. All subsequent analysis uses this artifact-filtered data, g_i.

We convert each artifact-filtered value, g_i, into a symbolized value, s_i, namely one of S different integers, 0,1, . . . , $S - 1$. Equiprobable symbols are formed by ordering all N of the base case artifact-filtered time-serial data points from the smallest to largest value. The first N/S of these ordered values correspond to the first symbol, 0. Ordered data values $(N/S) + 1$ through $2N/S$ correspond to the second symbol, 1, and so on. Equiprobable symbols have non-uniform partitions in the signal amplitude with the same occurrence frequency of g_i values by construction, and thus have no information about the PS structure. In contrast, symbols with uniform partitions (uniform symbols) have inherent dynamical structure before beginning the PS reconstruction. Thus, one advantage of equiprobable symbols is that dynamical structure arises *only* from the PS reconstruction, as described below. Moreover, large negative and large positive values of g_i have little effect on equiprobable symbolization, but dramatically change the partitions for uniform symbols. Information theoretic measures of the PS-DF (e.g., mutual information function) are smooth functions of the reconstruction parameters for equiprobable symbols, but are noisy functions of these same parameters for uniform symbols. Thus, in general, equiprobable symbols provide better discrimination of condition change than uniform symbols.

II.1 Conventional Statistical Measures (CSM)

CSM have long been used for general characterization. The most common statistical measures are the mean: $\bar{g} = \Sigma_i\, g_i/N$, where the sum over i, Σ_i, spans all N of the points in the analysis window, and the sample standard deviation, σ, which is defined as: $\sigma^2 = \Sigma_i\, (g_i - \bar{g})^2/(N-1)$. Higher moments about the mean include skewness: $s = \Sigma_i\, (g_i - \bar{g})^3/N\sigma^3$, and kurtosis, $k = \Sigma_i\, (g_i - \bar{g})^4/N\sigma^4 - 3$. A large positive (negative) value of skewness corresponds to a longer, fatter tail in the distribution about the mean to the right (left). Kurtosis measures the amount of flattening ($k < 0$) or excess peakedness ($k > 0$) about the mean. Another measure is the average number of time steps per wave cycle (frequently used in engineering analysis of sampled data): $m = N/[(n_c - 1)/2] \approx 2N/n_c$, for $n_c >> 1$ Here, n_c is the average number of mean crossings, and two successive mean crossings delimit one-half of a wave period. The first zero in autocorrelation function defined by $A(j) = \Sigma_i\, (g_i - \bar{g})(g_{i+j} - \bar{g}) / (N-j)\sigma^2$, is also a useful measure. While CSM are useful in the analysis of linear processes, they provide inconsistent discrimination for detection of condition change in nonlinear systems. We include them here for completeness and comparison.

II.2 Traditional Nonlinear Measures (TNM)

The advent and rapid development of nonlinear and chaotic dynamics over the last few decades has produced new and powerful measures for characterization via PS reconstruction [39, 42, 43], which uses time-delay vectors that are formed from the (symbolized) s_i-data, $y(i) = [s_i, s_{i+\lambda}, \ldots, s_{i+(d-1)\lambda}]$. The choice of lag, λ, and embedding dimension, d, determines how well the PS reconstruction unfolds the dynamics. Too high an embedding dimension could result in overfitting of real data with finite length and noise. Moreover, different observables of a system contain unequal amounts of dynamical information [77], implying that PS reconstruction could be easier from one variable, but more difficult or impossible from another. Our analysis seeks to balance these caveats for finite-length noisy data.

We use the term, "traditional nonlinear measures" (TNM), as distinct from the phase-space measures in the next subsection. We choose three of the most-frequently-used TNM, as potential indicators of dissimilarity, namely: (i) the first minimum in the mutual information function as a nonlinear measure of decorrelation time, (ii) the correlation dimension as a measure of complexity, and

(iii) the Kolmogorov entropy as a measure of predictability. We describe these measures next, with more detailed definitions and characterizations in the references cited below.

The mutual information function (MIF) measures average bits of information that can be inferred from one measurement about a second, as a function of the time delay between the two signals. Shannon and Weaver [78] developed the MIF, which was later applied to time series. [79] The first minimum in the MIF, M_1, is an average de-correlation time. The MIF is: $I(q, r) = I(r, q) = H(q) + H(r) - H(r, q)$, where H is entropy: $H(q) = -\Sigma_i P(q_i) \log_2[P(q_i)]$ and $H(q, r) = -\Sigma_i P(q_i, r_j) \log_2[P(q_i, r_j)]$. One set of signals is $Q = \{q_1, q_2, \ldots, q_N\}$, with associated occurrence probabilities, $P(q_1), P(q_2), \ldots, P(q_N)$. A second set of measurements is $R = \{r_1, r_2, \ldots, r_N\}$, with a time delay relative to Q, and with occurrence probabilities $P(r_1), \ldots, P(r_N)$. $P(q_i, r_j)$ is the joint probability that both states occur together.

The maximum-likelihood correlation dimension [80, 81] is: $D = -M\{\Sigma_{ij} \ln[(\delta_{ij}/\delta_0 - \delta_n/\delta_0)/(1 - \delta_n/\delta_0)]\}^{-1}$, where M is the number of randomly-sampled pairs of phase-space points. The maximum-norm distance between PS-point pairs, i and j, is $\delta_{ij} = \max(0 \le k \le m-1) |g_{i+k} - g_{j+k}|$, where m is the average number of data points per cycle, as defined above. The distance δ_n is the scale length that is associated with noise. Distances are normalized with respect to a nominal scale length, δ_0, as a balance between sensitivity to local dynamics (typically at $\delta_0 \leq 5a$) and avoidance of excessive noise (typically at $\delta_0 \geq a$). The symbol a denotes the absolute average deviation as an indicator of variability [81], $a = \Sigma_i |g_i - \bar{g}|/\mathrm{N}$.

The Kolmogorov entropy (K-entropy), K, is the rate of information loss per unit time (bits per second), and is the sum of the positive Lyapunov exponents. Positive, finite K is generally viewed as a clear indication that the process manifests chaotic dynamics. Extremely large entropy values indicate a stochastic (totally unpredictable) phenomenon. K is estimated from the average number of time steps, b_i, for two PS points, initially within $\delta \le \delta_0$, to diverge to $\delta > \delta_0$. We use the maximum-likelihood form of Schouten *et al.* [81], $K = -f_s \log(1 - 1/\underline{b})$, with $\underline{b} = \Sigma_i b_i/M$ for M point pairs. The data-sampling rate is f_s.

TNM capture nonlinear dynamical features, but do not offer a very sensitive tool for detection of dynamical *change*. The main reason is that TNM, like CSM, are expressed as a sum (or integral) over (a region of) the PS, which averages all dynamical details into one number. Consequently, two (very) different dynamical regimes may lead to very close, or even equal measures. Moreover, the usual definitions of K-entropy and correlation dimension are in the limit of zero scale length. However, all real data have noise, and even noiseless model data is limited by the finite precision computations. Thus, we use a finite length scale that is larger than the noise ($\delta_0 = 2a$), at which to report the values of K and D. Consequently, our values of K and D do not capture dynamical complexity at length scales smaller than δ_0 and have smaller values than expected for the zero-scale-length limit ($\delta_0 \to 0$).

II.3 Phase-Space Dissimilarity Measures

We addressed some of the limitations of CSM and TNM as discriminators of condition change by introducing phase-space dissimilarity measures (PSDM), [30-33] which we review briefly for the reader's convenience. The time-delay reconstruction of the symbolized data (as discussed above) partitions the phase-space (PS) into S^d hypercubes or bins. By counting the number of PS points that occur in each bin, we obtain the distribution function (DF) as a discretized density on the attractor. We denote the population of the jth DF bin, R_j, for the base case (nominal state), and S_j for a test case (off-normal state), respectively. Comparison of the test case to the base case involves measuring the difference between R_j with S_j by the χ^2 statistic and L_1 distance:

$$\chi^2 = \sum_j \left(R_j - S_j\right)^2 / \left(R_j + S_j\right), \tag{1}$$

$$L = \sum_j \left|R_j - S_j\right|. \tag{2}$$

The summations in Eqs. (1) - (2) run over all of the populated PS cells. The χ^2 statistic is one of the most powerful, robust, and widely used tests for dissimilarity between two DFs. This χ^2 is not an unbiased statistic for accepting or rejecting a null statistical hypothesis but rather is a *relative* measure [76] of dissimilarity between the two DFs. The L_1 distance is the natural metric for DFs by its direct relation to the total invariant measure on the attractor. These measures account for changes in the geometry and visitation frequency of the attractor. Consistent calculation obviously requires the same number of points in both the base case and test case DFs, identically sampled; otherwise the distribution functions must be properly rescaled.

The accuracy and sensitivity of the PS reconstruction can be enhanced by connecting successive PS points as prescribed by the underlying dynamics, $y(i) \rightarrow y(i + 1)$. Thus, we obtain a discrete representation of the process flow $Y(i) = [y(i), y(i + 1)]$ that is formed by adjoining two successive vectors from the d-dimensional reconstructed PS. $Y(i)$ is a $2d$-dimensional, connected-phase-space (CPS) vector. As before, R and S denote the CPS DFs for the base case and test case, respectively. We then define the measures of dissimilarity between these two CPS DFs via the L_1-distance and χ^2 statistic, as before [73, 74, 82-84]:

$$\chi_c^{\,2} = \sum_{jk} \left(R_{jk} - S_{jk}\right)^2 / \left(R_{jk} + S_{jk}\right), \tag{3}$$

$$L_c = \sum_{jk} \left|R_{jk} - S_{jk}\right|. \tag{4}$$

The subscript c denotes CPS measures; the subscripts, j and k, denote the initial, $y(i)$, and final, $y(i+1)$, PS states, respectively. The value $\lambda = 1$ results in $d - 1$ components of $y(i + 1)$ being redundant with those of $y(i)$; we allow this redundancy to accommodate other data such as discrete points from two-dimensional maps. CPS measures have higher discriminating power than their non-connected counterparts. Indeed, one can prove [73] that these measures satisfy the inequalities: $\chi^2 \le L$, $\chi_c^{\,2} \le L_c$, $L \le L_c$, and $\chi^2 \le \chi_c^{\,2}$.

We call the quantities in Eqs. (1) – (4), phase space dissimilarity measures (PSDM). Their definitions allow PSDM to flag transitions between regular and chaotic regimes, but also to discriminate well between different chaotic regimes. While straightforward methods exist [39, 42, 85] for discriminating between regular and chaotic motion, or for detecting the transition between these regimes, discriminating between close chaotic regimes (e.g., Lyapunov exponents, Kolmogorov entropy, correlation dimension, etc. [42, 43]). is almost impossible. The reason for the superior performance of PSDM is rather simple: TNM use a difference of averages, while PSDM use sums of the absolute value of differences.

The disparate range and variability of the PSDM make their interpretation and comparison rather difficult, especially for noisy data. We obtain a consistent means of comparison via renormalized dissimilarity measures (RDM) [73, 74], by proceeding as follows. If V denotes a dissimilarity measure from the set, $V = \{L, L_c, \chi^2, \text{and } \chi_c^{\,2}\}$, we obtain the mean value, $\overline{V}$, of the dissimilarity measure by comparison among the $B(B–1)/2$ unique combinations of the B base case cutsets, with a corresponding sample standard deviation σ_1. We subsequently compare each non-overlapping test case cutset to each of the B base case cutsets, and obtain the corresponding average dissimilarity value, V_i, of the ith cutset for each dissimilarity measure. The RDM of the measure V is defined as the number of standard deviations that the test case deviates from the base case mean, $U(V) = |V_i - \overline{V}|/\sigma_1$. A statistically significant trend in the RDM indicates abnormal dynamics for event forewarning.

The best choice of the parameter set, $\{N, w, S, d, B, \lambda\}$, depends not only on the system, but also on the specific data. We choose a "reasonable" value for the number, B, of base case cutsets, $5 \le B \le 10$, as a balance between a reasonably short quasi-stationary period of "normal" dynamics and a sufficiently long period for statistical significance. We find that timely forewarning is obscured by a value for N that is too large, while inadequate statistical sampling of the attractor occurs if N is too small.. Our analysis proceeds as follows: (a) choose the parameter set, $\{N, w, S, d, \lambda\}$; (b) compute the

renormalized PS dissimilarities for the specific data; and (c) systematically search over the parameters $\{N, w, S, d, \lambda\}$, to find the best forewarning indication.

Our previous work [30-33] found that RDM are sensitive measures of condition change, but that further improvements are needed to give an explicit indication of machine failure. Thus, we seek a more robust and specific end-of-life (EOL) forewarning. Extensive application of the PSDM approach [32, 33] shows that all four of the PSDM display similar trends, as illustrated by the analysis of the machine data below. This observation suggests the definition of a composite measure, C_i, as the sum of the four renormalized PSDM for the i-th dataset:

$$C_i = U(\chi^2) + U(\chi_c^2) + U(L) + U(L_c). \quad (5)$$

This composite measure is expected to be more robust than any one of the PSDM, while accurately indicating condition change. The EOL indication from this composite measure is then quantified as follows. We use contiguous, non-overlapping windows of C_i to obtain a least-squares straight-line fit:

$$y_i = ai + b. \quad (6)$$

The window length of $n = 10$ values of C_i (and y_i below) is chosen consistent with the number of cutsets in each snapshot ($B = 10$). Other values of B give inferior indication of condition change. Next, the variance, σ_2^2, measures the variability of the C_i values about this straight-line fit:

$$\sigma_2^2 = \Sigma_i (y_i - C_i)^2/(n\text{-}1). \quad (7)$$

G measures the variability of next n values of C_i about an extrapolation of this straight-line fit:

$$G = \Sigma_i (y_i - C_i)^2/\sigma_2^2. \quad (8)$$

Other fits (quadratic, cubic, and quartic) extrapolate poorly outside the fitting window.

The index, i, in Eqs. (6) – (8) runs over the B values of C_i and y_i. The quantity G is similar to a chi-squared statistic, but we do not use that notation to avoid confusion with the two χ^2 PSDM. A statistical test for G would involve (for example) the null hypothesis that deviations from the straight-line fit are normally distributed. Analysis of accelerated machine-test data uses Eqs. (5) – (8) to extract both forewarning and an indication of failure onset. We present the results of this analysis next.

III. APPLICATION TO MACHINE DATA

Without a model, the "correct" choice of process-indicative data can be justified only *a posteriori*. As a practical matter, this choice is limited to measurable process variables. Moreover, the analyst's choice must recognize that not all observables capture the same amount of information [77]. Typical data encountered in machine/industrial applications are tri-axial acceleration, $\vec{a}$, and three-phase electrical current, I_i, and voltage, V_i. From these data, we calculate the instantaneous mechanical (vibration) or electrical power, $P \propto \vec{a} \cdot \int \vec{a}\, dt$ or $\Sigma_i I_i V_i$, respectively. The use of vibration or electrical power is certainly not unique. Indeed, one component of acceleration (or current or voltage) may provide an adequate process-indicative signal to extract condition change. The use of power has the advantage that only one channel of data is analyzed, rather than analysis of several channels (e.g., three channels of acceleration, or six of I_i and V_i) to find the best signal for change discrimination. This paper presents details of the forewarning analysis via *vibration power*. Analyses of three-phase electrical power, and individual channels of current, voltage, acceleration, velocity, and torque are described in Refs. 31 and 33.

For this analysis, the datasets for each test in the sequence were concatenated into a single long dataset. We verify data quality by checking for: the proper number of data points, any intervals with unchanged signal amplitude, adequate sampling rate, excessive periodic content, excessive noise,

saturation at high or low limits as an indicator of improper data scaling, and consistent signal amplitude across datasets in the test sequence. Subsequent analysis uses only data that pass these quality tests.

The Electric Power Research Institute (EPRI) sponsored work on predictive maintenance for large motors, simulating common failures via seeded faults. [86] Present analyses use tri-axial (vibration) acceleration data from the inboard (IB) motor location, because all data from the outboard motor location failed the quality check. Data were recorded in 1.5-second snap-shots at 40 kHz (60,000 points per dataset). Our analysis averages the measures over five subsets ($B = 5$) of 12,000-points.

III.1 EPRI Air-Gap Seeded Fault

One EPRI test [86] involved operator-imposed air-gap offsets in the rotor-stator alignment. The test bed was a three-phase, 800-HP sleeve-bearing, form-wound Allis Chalmers induction motor, rated at 4160 volts and 100 amps at 60 Hz with 10 poles, 94 copper rotor bars, 40 stator slots, running at a normal speed of 710 RPM. The first dataset of test sequence involves the motor running in its nominal state. Two different air-gap offset seeded faults were then imposed via preinstalled jackscrews. The second dataset imposed a static inboard air-gap offset of 8 mils from the nominal value of 30 mils. The third dataset retained the first fault, and added a static outboard air-gap offset by 20% in the opposite direction from the inboard shift, resulting in the rotor being skewed relative to the stator. Figure 1a shows a 20-millisecond segment of vibration power data with complex, nonlinear features. The corresponding statistical measures (Figs. 1b-1e) and traditional nonlinear measures (Figs. 1e-1g) do not provide a clear indication of the increasing severity of the seeded fault. Figure 2 shows that all four phase-space dissimilarity measures rise linearly with increasing fault severity, yielding good change discrimination.

III.2 EPRI Rotor-Bar Seeded Fault

A second EPRI [86] test involved operator-imposed partial or total cuts in the rotor bars. The test bed was the same Allis Chalmers motor, as in Sec. III.1. The test sequence began with the motor running in its nominal state (first dataset), followed by progressively more severe broken rotor bars. The second dataset involved one rotor bar cross section cut 50% in half at the 11 o'clock position. The third dataset was for the same rotor bar now cut through 100%. The fourth dataset was for a second rotor bar cut 100% at the 5 o'clock position, exactly 180° from, in addition to the first rotor failure. The fifth dataset was for two additional rotor bars cut adjacent to the original 11 o'clock bar, with one bar cut on each side of the original, yielding four bars completely open. The complete test sequence then captured an exponentially growing fault, from nominal operation, to ½, to 1, to 2, to 4 broken rotors bars. Figure 3a shows a 20-millisecond segment of vibration power data with complex, nonlinear features. The corresponding statistical measures (Figs. 3b-3e) and traditional nonlinear measures (Figs. 3e-3g) do not provide a clear indication of the exponentially-growing severity of the seeded fault. Figure 4 shows that all four phase-space dissimilarity measures rise linearly with the increasing fault severity, thus yielding good change discrimination.

III.3 Analysis of Turn-to-Turn-Short Seeded Fault Data

A third EPRI test [86] involved operator-imposed turn-to-turn shorts in a motor. The test bed was a three-phase, 500-HP, sleeve-bearing, form-wound General Electric induction motor, rated for 4,000 volts at 60 Hz, with 84 rectangular copper rotor bars, 6 poles, and 108 stator slots, running at a nominal speed of 1,185 RPM. The first dataset was from the motor, running in its nominal state. A second dataset involved a turn-to-turn (2.70-ohm) short by installing a large screw between two turns. A third dataset involved a more severe turn-to-turn (1.35-ohm) short by installing a smaller screw between two turns. The analysis sequence goes from largest turn-to-turn resistance (infinite resistance, corresponding to no short), to smaller (2.7 ohms), to smallest (1.35 ohms), corresponding to increasing severity in the fault. Figure 5a shows a 20-millisecond segment of vibration power data with complex, nonlinear features. The corresponding statistical measures (Figs. 5b-5e) and traditional nonlinear

measures (Figs. 5e-5g) show some consistency with the increasing severity of the seeded fault. The minimum (P_N) rises and maximum (P_X) falls (Fig. 5b) monotonically over the test sequence. Kurtosis decreases and skewness increases monotonically (Fig. 5c) over the test sequence. Linear increases occur in the average number of time steps per cycle (Fig. 5d) over a very narrow range (7.2-7.6), and the first zero in the autocorrelation function (Fig. 5e). Figure 6 shows that all four phase-space dissimilarity measures rise linearly with the increasing fault severity, thus yielding good change discrimination.

III.4 Analysis of Gear-Failure Acceleration Data

The Pennsylvania State University (PSU) operates the Applied Research Laboratory [87], including the Mechanical Diagnostics Test Bed (MDTB). A 30-HP, 1750-RPM, alternating current (AC), electric motor drives a gearbox, which is loaded by a 75-HP, 1750-RPM AC (absorption) motor. A digital vector drive unit controls the current to the absorption motor for torque variation up to 225 ft-lbs. The MDTB can test gear ratios from 1.2:1 to 6:1 in the 5-20 HP range at 2 to 5 times the rated torque of single and double reduction industrial gearboxes. The motors and gearbox are mounted and aligned on a bedplate, which is mounted on isolation feet to prevent vibration transmission to the floor. The shafts are connected with both flexible and rigid couplings. Torque limiting clutches on both sides of the gearbox prevent transmission of excessive torque during a gear jam or bearing seizure. Torque cells on both sides of the gearbox directly monitor the loads. The protocol for this accelerated failure test involves a break-in period at the nominal (1X) load (530 ft-lbs) for one hour, followed by twice (2X) or three times (3X) the normal load, as shown in Table 1 for Run #36, which also includes the time to failure (T_{fail}). The EOL failures typically include pinion damage, broken teeth, and a sheared shaft. Ten-second snapshots of tri-axial accelerometer data were sampled at 52 kHz; see Table 1 for the interval ($\Delta\tau$) between each snapshot. We convert the accelerometer data during the overload period into vibration power for this analysis. As before, the CSM and TNM show little if any failure forewarning,[34] so we do not show them here.

Figure 7 shows that all four PSDM rise systematically (Figs. 7a - 7d) to provide failure forewarning. Indeed, the abrupt increase in all four PSDM at 160 hours clearly forewarns of the imminent failure. We obtain this forewarning by quantifying significant deviations from the general trend via application of Eqs. (5) - (8). Chi-squared statistical tables give a value of $G \leq 28.5$ for $n = 10$ degrees of freedom with a probability of one out of the 650 snapshots or ($1/650 \sim 1.5 \times 10^{-3}$). However, we observe many instances of $G>28.5$ (solid curve in Fig. 7f), arising from dynamical correlations in the accelerometer data, thus violating the requirement for independent, identically distributed samples.

Instead, we use G as a *relative* EOL measure. Although G varies erratically, we observe a systematic trend in the running maximum of G, G_{max}, as shown by the dashed curve in Fig. 7f, neglecting (for example) the first six G-values to avoid startup transients. This running maximum steadily increases in modest increments to 376 over the first 159.75 hours of the test, while intermediate values of G fall well below the running maximum. Subsequently, a large increase occurs in C_i at 160 hours, which produces a correspondingly large rise in G, and therefore in G_{max}. The resulting jumps in G_{max} are quantified by the chain curve (-.-) in Fig. 7f, as the ratio of the current maximum in G, $(G_{max})_k$, to the previous maximum in G, $(G_{max})_{k-1}$, $R = (G_{max})_k/(G_{max})_{k-1}$. G rises to 2,493 at 160 hours, with a corresponding ratio, $R = 6.62$, while the largest non-EOL ratio is $R = 2.22$ at 28.5 hours. We find that the forewarning values of C_i across the various MDTB tests are not consistent, but that the values of G_{max} and R consistently provide both forewarning of the failure and indication of the failure onset, as shown in Table 1: (a) the largest non-EOL value of R (R_{NEOL}) and the corresponding value of G (G_{NEOL}); (b) values of R (R_{EOL}) and G (G_{EOL}) that indicate the end of life, and the matching time (T_{EOL}/T_{FAIL}); (c) the value of G at failure onset (G_{ONSET}) and the corresponding time (T_{ONSET}/T_{FAIL}); and (d) the failure-endpoint time (T_{FAIL}).

Table 1 also shows results for Runs #37-38. The corresponding plots [33] are very similar to Fig. 7 and are not shown. Runs #36-38 have largest non-EOL values: $R_{\mathrm{NEOL}} = 6.20$ and $G_{NEOL} = 376$. The smallest EOL values are: $R_{\mathrm{EOL}} = 6.62$ and $G_{EOL} = 2{,}493$. Thus, limits (for example) of $R > 6.4$ and $G >$

1,800 provide EOL forewarning. Moreover, we find that the largest EOL value of G_{EOL} = 13,486, while the smallest failure-onset value is G_{ONSET} = 16,284. Thus, an intermediate value (for example) of G > 15,000 distinguishes the EOL from failure onset forewarning. This approach gives quantitative limits for transitions from nominal operation (green-light for "go" in a traffic signal metaphor), to forewarning of failure (yellow light for "caution"), and to failure onset (red-light for "stop").

MDTB Run #39 involves a different test protocol: a one-hour break-in period at nominal load (1X), followed by 2X load for two hours, after which the load alternates between 3X and 2X loads for ten and five minutes, respectively. Figures 8-9 show the Run #39 PSDM for the 2X and 3X overload, respectively. The sawtooth features in each of the subplots correspond to the transition between 2X and 3X loads; the straight-line portion in Fig. 8 corresponds to the 2X segment in Fig. 9, and inversely. Run #39 seeks failure forewarning in the presence of load changes. Table 1 shows that the above limits for G and R also distinguish between the non-EOL (green) and EOL (yellow) states for the 3X-portion of this test, because the higher overload drives the failure. These limits do not apply to the 2X test, due to the reduced damage at the lower overload. Unsurprisingly, a different limit of G > 38,000 (for example) distinguishes between the EOL and failure onset forewarnings, due to the change in test protocol. The green-yellow-red approach still applies for this test.

III.5 Analysis of Shaft-Crack Seeded Fault

We analyzed additional PSU seeded-fault data with a progressively increasing depth of cut at the base of a motor-driven rotor blade. This test sequence simulates the growth of a crack in a turbo-machine, which eventually causes failure. The rotor is driven at a fixed rotational speed by a fractional horsepower DC motor that was made by Bodine Electric Company, with typical electrical values of 4 volts and 2 amps. Test data at each depth of cut were tri-axial accelerations in three orthogonal directions on one bearing pillow block. The sequence test states were: (a) nominal operation with no cut, (b) successively deeper cuts through one of eight equi-angularly-spaced 5/8"-diameter shafts that were fixed perpendicular to the rotation axis of the motor-driven rotor. The cut depths range from 1/16" to 3/8". Figure 10 shows a resultant segment of vibration power (Fig. 10a), along with conventional statistical measures (Figs 10b-10e), and traditional nonlinear measures (Fig. 10e – 10g). The magnitudes of minimum and maximum in vibration power (Fig. 10b) are constant, then rise abruptly for the deepest cut. The number of time steps per cycle (Fig. 10d) rises slowly and monotonically, also showing a large increase for the largest cut depth. None of the other measures in Fig. 10 show a consistent change over this test sequence. Figure 11 shows that all four PSDM rise monotonically by one-hundred-fold as the cut depth increases from zero (baseline) to 3/8". These strong indications of change are in sharp contrast to the weak ones of Fig. 10.

IV. APPLICATION TO PHYSIOLOGICAL DATA

IV.1 Analysis of EEG Data

We present five illustrations of our approach by comparing traditional nonlinear measures (D and K) with phase-space dissimilarity measures (χ^2 and L_1). As discussed in Sect. II.3, direct comparison of these measures is difficult due to their disparate range, variability, and physical meaning. Consequently, renormalization of the PSDM allows meaningful comparison by defining V_i as the value of each indicator for the i-th cutset from the set, $V = \{D, K, \chi^2, \text{and } L\}$. The remainder of the RDM analysis remains the same as before. Dynamical states close to (far from) the baseline have small (large) values of the renormalized dissimilarity.

Human electroencephalogram data were acquired during clinical epilepsy monitoring and analyzed by the procedure of Section II. Figure 12 shows typical results. Raw data in subplot (a) have very complex, non-periodic features that are typical of brain waves. The seizure event occurred at 110.7 minutes, as denoted by the solid vertical line in subplots (d) and (e). No seizure event forewarning is provided by the correlation dimension in subplot (b), or by the Kolmogorov entropy in subplot (c). The isolated peaks at 42 and 58 minutes in subplot (c) are not significant. An event forewarning of 27

minutes is provided by $U(\chi^2)$ in subplot (d) and $U(L)$ in subplot (e), with two (or more) successive occurrences above the threshold of 5 (dashed horizontal line) at 85 minutes (vertical dashed line). Hively and Protopopescu (2003) give additional details of the methodology for this and subsequent examples. Our most recent results give a total true rate of 56/60 with up to 5 hours forewarning via analysis of two bipolar EEG scalp channels. [72]

IV.2 Analysis of EKG Data for Ventricular Fibrillation

Human electrocardiogram data were acquired during ambulatory monitoring. Figure 13 shows results for a ventricular fibrillation event at 37 minutes. The raw data in subplot (a) show ten distinct heartbeats and their associated quasi-periodic (nonlinear) features. The correlation dimension in subplot (b) varies randomly (no forewarning features) with a rise at the fibrillation event. The Kolmogorov entropy in subplot (c) varies erratically; the isolated peaks occurring at 8 and 24 minutes are not valid forewarning indications. Event forewarning of 16 minutes (the vertical dashed line) is provided by both $U(\chi^2)$ in subplot (d) and $U(L)$ in subplot (e); forewarning corresponds to two (or more) successive occurrences above the threshold (dashed horizontal line). Similar results were obtained for several additional datasets.

IV.3 Analysis of EKG Data for Syncope

Human electrocardiogram data were acquired during laboratory tests of fainting (syncope), under the following protocol: (i) lying horizontal for 10 minutes, (ii) lying in tilted condition (70^o from horizontal) for 40 minutes, and (iii) lying horizontal again for 5 minutes. Figure 14 (top) shows non-syncopal results with low values of renormalized dissimilarity (~10) that increase very slowly and erratically over the tilt period (slope, A~0.06-0.07 per minute). Figure 14 (bottom) shows syncopal results for the same subject with much larger renormalized dissimilarity (40-70) that increase much more rapidly over the tilt period (A~0.8-1 per minute). The tilt period in this second test was terminated early when the subject fainted. Similar results are obtained for a second subject.

IV.4 Analysis of EKG Data for Sepsis

Heart wave data were obtained via surface chest electrodes from anesthetized rats subjected to an induced sepsis experiment. After 55 minutes of normal-state recording, each test rat was exposed to inhaled bacterial endotoxin that induces an inflammatory response and eventually sepsis. Figure 15 shows sample results. Raw data in subplot (a) have distinct heartbeats with additional quasi-periodic (nonlinear) features. No indication of condition change is displayed by either the correlation dimension in subplot (b), or by the Kolmogorov entropy in subplot (c). The condition change is shown clearly by both $U(\chi^2)$ in subplot (d) and $U(L)$ in subplot (e), which remains low for the first 57 minutes, rising abruptly after the exposure onset, remaining high for the next 20 minutes, then decreasing slowly as the immune response fought off the bioagent effects. This recovery response is consistent with other physiological observations during the test (not shown). The total true (negative) positive rate for (un)exposed animals is (6/6) 17/17.

IV.5 Analysis of Lung Sounds

A surface stethoscope acquired lung sounds data during lung experiments on anesthetized pigs. The baseline state consisted of normal breathing. Subsequent test cases were obtained by injecting a controlled volume of air (in increments of 100 milliliters up to 1400 milliliters) in the space between the diaphragm and the lungs, making breathing increasingly more difficult. Figure 16 shows sample pneumothorax results. Raw lung sounds data in subplot (a) have very complex features, including quasi-periodic heartbeats that are superimposed on slow breath-cycle undulations. The correlation dimension in subplot (b) provides no clear indication of condition change. The Kolmogorov entropy in subplot (c) likewise varies erratically. Condition change is indicated by both $U(\chi^2)$ in subplot (d) and $U(L)$ in subplot (e); both rise to a plateau of 5 over 100-500 ml, then increase to values larger than 20

over 500-1300 ml thereby providing robust forewarning of the animal's death at 1400 ml. Similar results were obtained for a second animal.

V. DISCUSSION and CONCLUSIONS

We have developed a model-independent method to quantify condition change from complex, time-serial data. First, we use a novel zero-phase quadratic filter to remove confounding artifacts (such as sinusoidal periodicity from three-phase electrical signals, and eye-blinks or breathing from biomedical data). The artifact-filtered data are converted into a statistical distribution function that describes the visitation frequency and sequence of the dynamical states. Dissimilarity measures between baseline and test distribution functions (DFs) detect condition change by summing the absolute values of the differences between DFs. The methodology is quite general, and we illustrate its usefulness by quantifying change for a variety of machine and physiological events. Success for these diverse applications provides confidence that this approach is useful for detecting condition change in nonlinear and chaotic processes for both machine and biomedical applications.

Examples of machine failure forewarning include: detecting balanced and unbalanced centrifugal pump conditions from motor power; [30] distinguishing different drilling conditions from spindle motor current of a machining center; [30] and predicting failure of a bellows coupling in a rotating drive train from motor current; [88] discerning the difference in micro-cantilever vibrations with and without mercury on the sensor; forewarning of failure in electrical motors (Figs. 1-6) from vibration power and motor power; [33] and forewarning of failure in motor-driven components from vibration power (Figs. 7-11) and motor power. [33] Table 2 summarizes recent results for forewarning of seeded faults and accelerated failures in various machines and equipment. We compare conventional statistical measures (CSM), traditional nonlinear measures (TNM), and phase-space dissimilarity measures (PSDM) as indicators of condition change. CSM include minimum, maximum, average, sample standard deviation, skewness, kurtosis, average time steps per cycle, and first zero in the auto-correlation function. TNM include first minimum in the mutual information function as a measure of decorrelation time, correlation dimension as a measure of complexity, and Kolmogorov entropy as a measure of information loss rate. PSDM are the χ^2 statistic and L_1 distance between the time-delayed reconstructions of the PS-distribution functions on the discretized attractor. PSDM show more consistent and better discriminating power for timely forewarning of failure or abnormal conditions, than either CSM or TNM. The reason for the improved performance of PSDM is rather simple. CSM and TNM compare averages, while PSDM are the sum over the absolute difference between the two phase-space states. In addition, the enhanced discrimination facilitates use of PSDM on noisier data.

Examples of physiological-event forewarning include: brain waves for forewarning of epileptic events (Fig. 12); heart waves for forewarning of ventricular fibrillation (Fig. 13), and for detection of syncope (Fig. 14) and sepsis (Fig. 15); and lung sounds for detection of breathing difficulty (Fig. 16). The dissimilarity measures have small values in the normal state, followed by significantly larger values above a “normality threshold,” indicating abnormal dynamics. The results show that the phase-space dissimilarity approach is sensitive, robust, and timely. PSDM show consistently better forewarning than either CSM or TNM for physiological applications.

We now have high-fidelity laboratory integration of the technology elements into desktop-computer software that analyzes noisy, archival data and provides indication of condition change. The analysis is much faster than real-time (e.g., less than 12 hours of CPU time on a P4 desktop computer to analyze 261 hours of 19-channel EEG data),[60] and can handle multiple channels.[72]

We deem these results as encouraging and worthy of continuing development despite several limitations, which we discuss next. First, we use all of the data as a training set, limiting the strength of our conclusions. However, the alternative would involve equally-sized training and test sets. The resultant training (and test) sets would result in inadequate statistics. Second, we analyze both the machine and physiologic data from controlled tests, rather than an uncontrolled, real-world

environment. Third, our results depend on careful adjustment of the analysis parameters for the best total-true rate. Fourth, we analyze only physician-selected portions of the EEG data, rather than the full monitoring period. Fifth, these results are for only a limited number of datasets (e.g., a total of sixty EEG datasets, forty with epileptic events for a single seizure type, temporal lobe epilepsy). Much more data (hundreds of datasets) are needed for the proper choice of the analysis parameters as part of a robust and conclusive statistical validation. These data requirements are far beyond our present capabilities, and almost everyone else's, based on present publications. Sixth, we have not performed prospective analysis of long-term continuous data, which is the acid test for any predictive approach. Seventh, the present analyst-intensive methodology uses retrospective analysis of archival data on a desktop computer. Real-world forewarning requires analyst-independent, prospective analysis of real-time data on a portable device. Clearly, much work remains to address these issues. Thus, we view the importance of this work as examples of the overall potential of the methodology, rather than the specific results.

Finally, we note the recent implementation of the PSDM analysis on a hand-held device [89] (personal digital assistant), which is much more appropriate for real-world use. This success provides a portable monitor for many new directions for future research and development. Moreover, an advanced monitor might include a mobile phone and global-positioning system to call responders automatically to the event location. These developments would allow (for example) failure forewarning in critical equipment (e.g., motors and motor driven components) at industrial and remote locations (e.g., motor-driven turbine-generator at a natural gas pumping station). Many potential biomedical applications exist: epilepsy diagnosis, pre-surgical monitoring, out-patient ambulatory forewarning, monitoring for drug trial efficacy, use in conjunction with function imaging (e.g., fMRI), and use in conjunction with Vagal nerve simulation for seizure control; stoke detection via EEG and ECG in high-risk individuals; early diagnosis of Parkinson's disease and other brain disorders; diagnosis of CNS pathologies via analysis of sensory-evoked potential changes in EEG; diagnosis of head trauma via EEG changes; hands-free computer control via removal of confounding artifacts (e.g., eye-blink and other facial muscle activity) from scalp EEG; Cochlear-implant monitor via analysis of EEG and imposed sounds to evaluate the brain's processing of signals if hearing is not restored; drug/chemical effects diagnosis via EEG changes; motion disorder management by EEG analysis for onset detection, followed by deep brain stimulation and/or trans-spinal drug infusion; detection of brain ischemia (loss of blood flow) during brain surgery; drowsiness monitor via extraction of eye-blinks (an indicator of sleepiness) from scalp EEG; fitness-for-duty monitor for key personnel in high stress situations via scalp EEG analysis; automated sleep staging of nighttime polysomnogram data in outpatients; daytime sleepiness monitor of ambulatory outpatients for a sleep disorders; cardiac diagnosis of ambulatory outpatients via ECG analysis on an advanced Holter monitor; forewarning of cardiac events in ambulatory outpatients; forewarning of cardiac events during transport by an emergency responder; fetal ECG monitor during labor and delivery; monitor for premature and newborn infants with an elevated risk for cardiovascular events or sudden infant death syndrome via ECG, EEG, and/or chest sounds; forewarning of heart valve failure via ECG or chest sounds; fainting (syncope) monitor via ECG analysis for susceptible patients; shock monitor via ECG/EEG analysis for trauma patients; forewarning of impending rapture of an abdominal aortic aneurism via analysis of ECG, abdominal sounds, and/or aortic stress-strain data; diagnosis of lung disorders via analysis of chest sounds; forewarning/detection of an asthma attack via chest-sounds; detection of excessive wear, infection, bone degeneration, and related abnormalities in patients with orthopedic implants via joint sounds and/or muscle activity; artificial-heart monitor via analysis of chest sounds and/or electrical activity to adjust pumping effort for metabolic demand and forewarn of pump failure; continuous blood-glucose monitor via skin-mounted optical-sensor for automatic control of insulin infusion and/or other therapeutic agents; personal monitor for dementia-sufferers at home via multiple sensors (e.g., EEG, ECG, and chest sounds) to provide early detection of illness and/or forewarning of catastrophic health events, as above; monitor for nursing home and assisted-care residents via EEG, ECG, pulse oximetry, body temperature; soldier monitor via clothing-embedded sensors for battlefield assessment of the physiological state; and sports-fitness monitor via ECG and chest sounds to assess training results in terms of healthy variability. The possibilities are manifold for a suitably refined condition-change-indication device.

Acknowledgments

This work was supported in part by the U.S. Department of Energy's Materials Science and Engineering Program of the Office of Basic Energy Sciences, the Nuclear Energy Research Initiative (project# NERI2000-109), and the Laboratory Directed Research and Development Program at the Oak Ridge National Laboratory, which is managed by UT-Battelle, LLC, for the USDOE under Contract No. DE-AC05-00OR22725. ViaSys Healthcare Inc. (formerly Nicolet Biomedical Inc. of Madison, WI), provided human brain wave data under Cooperative Research and Development Agreement #99-0559 and Physio-Control Corp. supplied human heart wave data under Cooperative Research and Development Agreement #95-0353. We thank Drs. Jan Stein (Electric Power Research Institute) and Karl Reichard (Applied Research Laboratory at Pennsylvania State University) for providing machine data.

REFERENCES

1. NIST/ATP Workshop on Condition-Based Maintenance, http://www.nist.gov/www/cbm/cbm_wp1.htm.

2. B. S. Berger, M. Rokni, and I. Minis, Int. J. Engng. Sci. **30**, 1433 (1992).

3. S. T. S. Bukkapatnam, A. Lakhtakia, and S. R. T. Kumara, Phys. Rev. E **52,** 2375 (1995).

4. S. T. Chiriacescu, Stability in the Dynamics of Metal Cutting, Studies in Applied Mechanics vol. **22,** Elsevier, New York, 1990.

5. G. Giacomelli and A. Politi, Phys. Rev. Lett., **76**, 2686 (1996).

6. I. Grabec, Phys. Lett., A **117,** 384 (1986).

7. I. Grabec, Proc 8th Int. Acoustic Emissions Symp., p. 87, Tokyo, Japan, 1986.

8. I. Grabec, Int. J. Mach. Tools Manufact., **28,** 19 (1988).

9. C. Hualing and D. Depei, "A new theoretical model of nonlinear chatter in cutting process," Proc. 11th Int. Conf. Production Res. (ICPR), p. 932 (1991).

10. K. Jemielniak and A. Widota, Int. J. Mach. Tools Manufact., **29**, 249 (1989).

11. R. I. King, "Historical Background," Chapter 1 in Handbook of High-Speed Machining Technology, R.I. King ed., Chapman and Hall Publ., New York, 1985.

12. F. Koenigsberger and J. Tlusty, Machine Tool Structures--Volume 1, Pergamon Press, New York, 1970.

13. J. S. Lin and C. I. Weng, Int. J. Mach. Tools Manufact., **30**, 53 (1990).

14. J.,S. Lin and C.,I. Weng, Int. J. Mech. Sci., **8**, 645 (1991).

15. F. C. Moon, "Chaotic Dynamics and Fractals in Material Removal Processes," Chapter 2 of Nonlinearity and Chaos in Engineering Dynamics, ed. J.M.T. Thompson and S.R. Bishop, John Wiley and Sons, New York, 1994.

16. L. Qu, A. Xie and X. Li, Mech. Mach. Theory, **28**, 699 (1993).

17. G. Stépán, Retarded dynamical systems: stability and characteristic functions, Pitman Res. Notes in Mathematics, vol. 210, John Wiley and Sons, New York, 1989.

18. J. Tlusty, "Machine Dynamics," Chapter 3 of Handbook of High-Speed Machining Technology, R. I. King ed., Chapman and Hall Publ., New York, 1985.

19. J. Tlusty and F. Ismail, Annals CIRP, **30**, 299 (1981).

20. J. Tlusty and M. Poláček, Proc. 9th MTDR Conf., p. 521, Pergamon Press, 1968.

21. S. A. Tobias, Machine-Tool Vibration, John Wiley and Sons, New York, 1965.

22. Y.. Ueda and H. Ohta, and H. B. Stewart, Chaos, **4**, 75 (1994).

23. D. B. Welbourn and J. D. Smith, Machine-Tool Dynamics--An Introduction, Chapters 4-5 (Cambridge University Press, 1970).

24. D. W. Wu and C. R. Liu, J. Engng. for Industry, **107,** 107 (1985).

25. D. W. Wu and C. R. Liu, J. Engng. for Industry, **107**, 112 (1985).

26. S. Smith and J. Tlusty, Annals CIRP, **41**, 433 (1992).

27. R. Teltz and M.A. Elbestawi, Trans. ASME, **115**, 122 (1993).

28. L. M. Hively, N. E. Clapp, and C. S. Daw, "Nonlinear Analysis of Machining Data," ORNL/TM-13157 (Oak Ridge National Laboratory, Oak Ridge, TN, January 1996).

29. L. M. Hively, V. A. Protopopescu, N. E. Clapp, and C. S. Daw, "Prospects for Chaos Control of Machine Tool Chatter," ORNL/TM-13283 (Oak Ridge National Laboratory, Oak Ridge, TN, June 1998).

30. L. M. Hively, "Data-Driven Nonlinear Technique for Condition Monitoring," Proc. Maintenance and Reliability Conf. **1,** 16.01-16.10 (Univ. of Tennessee, Knoxville, TN, 1997).

31. L. M. Hively, V. A. Protopopescu, M. Maghraoui, and J. W. Spencer, "Annual Report for NERI Proposal #2000-0109 on Forewarning of Failure in Critical Equipment at Next-Generation Nuclear Power Plants," ORNL/TM-2001/195 (Oak Ridge National Laboratory, Oak Ridge, TN, September 2001).

32. L. M. Hively and V. A. Protopopescu, "Forewarning of Failure in Critical Equipment at Next Generation Nuclear Power Plants," ORNL/TM-2002/183 (Oak Ridge National Laboratory, Oak Ridge, TN, December 2002).

33. L. M. Hively, V. A. Protopopescu, K. M. Reichard, and, K. P. Maynard, "Failure Forewarning in NPP Equipment – NERI2000-109 Final Project Report," ORNL/TM-2003/222 (Oak Ridge National Laboratory, Oak Ridge, TN, 2003).

34. C. Caravati, F. Delogu, G. Cocco, and M. Rustici, Chaos **9**, 219 (1999).

35. G. Manal, F. Delogu, and M. Rustici, Chaos **12,** 601 (2002).

36. F. Pfeiffer, Chaos **4**, 693 (1994).

37. S. S. Viglione and G. O. Walsh, Proceedings: epileptic seizure prediction. Electroencephalogr Clin Neurophysiol., **39**, 435 (1975).

38. J. M. T. Thompson and H. B. Stewart, Nonlinear Dynamics and Chaos, John Wiley, Chichester, 1986.

39. J. P. Eckmann and D. Ruelle, Rev. Mod. Phys. **57**, 617 (1985).

40. E. A. Jackson, Perspectives of Nonlinear Dynamics, Vol. 1. Cambridge: Cambridge University Press, 1989; vol. 2, 1990.

41. S. H. Strogatz, Nonlinear dynamics and chaos, Reading: Addison Wesley, 1994.

42. H. D. I. Abarbanel, Analysis of Observed Chaotic Data, Springer, New York, 1996.

43. H. Kantz and T. Schreiber, Nonlinear Time Series Analysis, Cambridge University Press, 1997.

44. D. Ruelle, Chaotic Evolution and Strange Attractors, Cambridge University Press, Cambridge, 1989.

45. A. Babloyantz and A. Destexhe, Proc Natl Acad Sci USA, **83**, 3513 (1986).

46. Babloyantz A., in: Basar E, ed. Chaos in brain function. New York: Springer Verlag, 1990, p.42 and p.83.

47. D. K. Ivanov, H. A. Posch, and C. Stumpf, Chaos, **6**, 243 (1996)..

48. J. Jeong J, M. S. Kim, and S. Y. Kim, Phys Rev E **, 60,** 831 (1999).

49. V. Gribkov and D. Gribkova, Phys Rev E, **61**, 6538 (2000).

50. K. K. Jerger, T. I. Netoff, J. T. Francis, T. Sauer, L. Pecora, S. L. Weinstein, and S. J. Schiff, J Clin Neurophysiol.,**18**,259 (2001).

51. Lehnertz K, Andrzejak RG, Arnhold J, Kreuz T, Mormann F, Reike C, Widman G, and Elger CE., J Clin Neurophysiol **18**, 209 (2001).

52. Le Van Quyen M, Martinerie J, Navarro V, Baulac M, and Varela FJ.,. J Clin Neurophysiol **18**,191 (2001).

53. Osorio I, Harrison MAF, Lai Y-C, and Frei MG., J Clin Neurophysiol, **18**, 269 (2001)

54. Protopopescu V A, Hively LM, and Gailey PC., J Clin Neurophysiol., **18**, 223 (2001).

55. Sunderam S, Osorio I, Frei M. G, and Watkins J. F. III., J Clin Neurophysiol., **18**, 275 (2001).

56. Litt B and Echauz J, Lancet Neurology, **1**, 22 (2002).

57. Chavez M, Le Van Quyen M, Navarro V, Baulac M, and Martinerie J., IEEE Trans. Biomed. Eng.**, 50,** 537 (2003).

58. D'Alessandro M, Esteller R, Vachtsevanos G, Hinson A, Echauz J, and Litt B, IEEE Trans Biomed Eng**., 50,** 603 (2003).

59. H. Witte, L. D. Iasemidis, and B. Litt, IEEE Trans Biomed Eng., **50**, 537 (2003).

60. L. M. Hively and V. A. Protopopescu, IEEE Trans. Biomed. Engr. **50** , 584 (2003).

61. L. D. Iasemidis, IEEE Trans Biomed Eng., **50**, 549 (2003).

62. L. D. Iasemidis, D-S. Shiau, W. Chaovalitwongse, J. C. Sackellares, P. M. Pardalos, J. C. Principe, P. R. Carney, A. Prasad, B. Veeramani, and K. Tsakalis, IEEE Trans Biomed Eng., **50**, 616 (2003).

63. F. H. Lopes da Silva, W. Blanes, S. N. Kalitizin, J. Parra, P. Suffczynski, and D. N. Velis, IEEE Trans Biomed Eng 2003;50:540-8.

64. P. E. McSharry, L. A. Smith, and L. Tarassenko, IEEE Trans. Biomed. Eng., **50** , 628 (2003).

65. S. V. Notley and S. J. Elliott, IEEE Trans Biomed Eng**., 50**, 594 (2003).

66. J. S. Paul, C. B. Patel, H. Al-Nahash, N. Zhang, W. C. Ziai, M. A. Mirski, and D. L. Sherman, IEEE Trans. Biomed. Eng., **50,** 640 (2003).

67. C. Rieke, F. Mormann, R. G. Andrzejak, T. Kreuz, P. David, C. E. Elger, and K. Lehnertz, IEEE Trans Biomed Eng**., 50,** 634 (2003).

68. M. W. Slutzky, P. Cvitanovic, and D. J. Mogul, *IEEE Trans Biomed Eng*., **50**, 559 (2003).

69. L. M. Hively, N. E. Clapp, C. S. Daw, and W. F. Lawkins, "Nonlinear analysis of EEG for epileptic events," *ORNL/TM-12961* (Oak Ridge National Laboratory, Oak Ridge, TN, 1995).

70. L.M. Hively and V. A. Protopopescu, Chaos **14** , 408 (2004).

71. L .M. Hively and V. A. Protopopescu, "Advanced Physiological Monitoring of FCS Soldiers," Proc. 24th Army Sci. Conf. (Orlando, FL) Dec. 2004.

72. L. M. Hively, V. A. Protopopescu, and N. B. Munro, "Enhancements in Epilepsy Forewarning via Phase-Space Dissimilarity," under review for publication in J. Clin. Neurophysiol. (2004).

73. L. M. Hively, V. A. Protopopescu, and P. C. Gailey, Chaos **10**, 864 (2000).

74. V. A. Protopopescu, L. M. Hively, and P. C. Gailey, J. Clin. Neurophysiol. **18**, 223 (2001).

75. L. M. Hively and V. Protopopescu, "Detection of Dynamical Change in Physiological Time Series," Proc. Nucl. Math. Comp. Sci. (Amer. Nucl. Soc. LaGrange, IL, 2003).

76. l. M. Hively, P. C. Gailey, and V. A. Protopopescu, Phys. Lett. A **258**, 103 (1999).

77. C. Letellier, J. Maquet, L. Le Sceller, G. Gouesbet, and L. A. Aguirre, J. Phys. A. **31**, 7913 **(**1998); see also C. Letellier and L. A. Aguirre, Chaos **12**, 549 (2002).

78. C. E. Shannon and W. Weaver, The Mathematical Theory of Communication, Univ. of Illinois Press, Urbana, 1949.

79. A. M. Fraser and H. L. Swinney, Phys. Rev. A **33**, 1134 (1986).

80. F. Takens, Lecture Notes in Mathematics **1125**, 99 (1984).

81. J. C. Schouten, F. Takens, and C. M. van den Bleek, Phys. Rev. E **50**, 1851 (1994); J. C. Schouten, F. Takens, and C. M. van den Bleek, Phys. Rev. E **49**, 126 (1994).

82. P. C. Gailey, L. M. Hively, and V. A. Protopopescu, "Robust detection of dynamical change in scalp EEG," in Proc. Fifth Experimental Chaos Conference (June 28 - July 1, 1999, Orlando, Florida).

83. L. M. Hively, P. C. Gailey, and V. A. Protopopescu, in Proc. International Workshop: ''Chaos in Brain?,'' p. 333 (Bonn, Germany, 10–12 March, 1999), ed. K. Lehnertz et al. (World Scientific, Singapore, 2000),.

84. V. Protopopescu, L. M. Hively, and P. C. Gailey, Proc. 18th Energy Symp. on Energy Sci., p. 137 (May 15-16, 2000, Argonne, IL).

85. A. Cover, J. Reneke, S. Lenhart, and V. Protopopescu, Math. Models and Meth. in Appl. Sci. **7**, 823 (1997).

86. Electric Motor Predictive Maintenance Program, EPRI, Palo Alto, CA (1999) TR-108773-V2.

87. http://muri.arl.psu.edu/shared_data_repository.html

88. S. C. Robinson, T. W. Ayers, H. D. Haynes, L. M. Hively, R. E. Pollard, R. Curless, and K. Ziegler, CRADA Final Report for CRADA Number Y1295-0357 – High Throughput and Reliability (HiTaR), Y/DX-2365, Y-12 Plant, Oak Ridge, TN (15 July 1998).

89. L. M. Hively, K. L. Kruse, N. B. Munro, and V. A. Protopopescu, "Epilepsy Forewarning Using a Hand-Held Device," ORNL/TM-2005/40 (February 2005) Oak Ridge National Laboratory, Oak Ridge, TN.

==========

Table 1: Summary of MDTB Test Results[70]

Run	**Over-load**	**$\Delta\tau$** min	R_{NEOL}	G_{NEOL}	R_{EOL}	G_{EOL}	$\frac{T_{EOL}}{T_{FAIL}}$	G_{ONSET}	$\frac{T_{ONSET}}{T_{FAIL}}$	T_{FAIL} hr.
36	2X	15	2.22	376	6.62	2,493	0.985	244,655	0.998	162.50
37	3X	1	1.79	333	8.07	2,690	0.956	16,284	0.996	8.55
38	3X	1	6.20	374	11.71	13,486	0.938	48,379	0.990	4.02
39	2X	1	2.32	853	3.89	5,231	0.980	5,231	0.980	8.60
39	3X	1	2.88	1,151	29.03	33,415	0.972	44,552	0.994	8.60

Table 2: Summary of Recent Machine Failure Forewarning Results

Data Provider	*Equipment and Type of Failure*	*Diagnostic Data*	*Reference*
1) EPRI (S)	800-HP electric motor: air-gap offset	motor power	32
2) EPRI (S)	800-HP electric motor: broken rotor	motor power	32
3) EPRI (S)	500-HP electric motor: turn-to-turn short	motor power	32
4) Otero/Spain (S)	¼-HP electric motor: imbalance	acceleration	32
5) PSU/ARL (A)	30-HP motor: overloaded gearbox	load torque	32
6) PSU/ARL (A)	30-HP motor: overloaded gearbox	vibration power	32
7) PSU/ARL (A)	30-HP motor: overloaded gearbox	vibration power	32
8) PSU/ARL (S)	crack in rotating blade	motor power	32
9) PSU/ARL (A)	motor-driven bearing	vibration power	32
10) EPRI (S)	800-HP electric motor: air-gap offset	vibration power	present work
11) EPRI (S)	800-HP electric motor: broken rotor	vibration power	present work
12) EPRI (S)	500-HP electric motor: turn-to-turn short	vibration power	present work
13) PSU/ARL (A)	30-HP motor: overloaded gearbox	vibration power	present work
14) PSU/ARL (A)	30-HP motor: overloaded gearbox	vibration power	present work
15) PSU/ARL (A)	30-HP motor: overloaded gearbox	vibration power	present work
16) PSU/ARL (A)	30-HP motor: overloaded gearbox	vibration power	present work
17) PSU/ARL (S)	crack in rotating blade	vibration power	present work

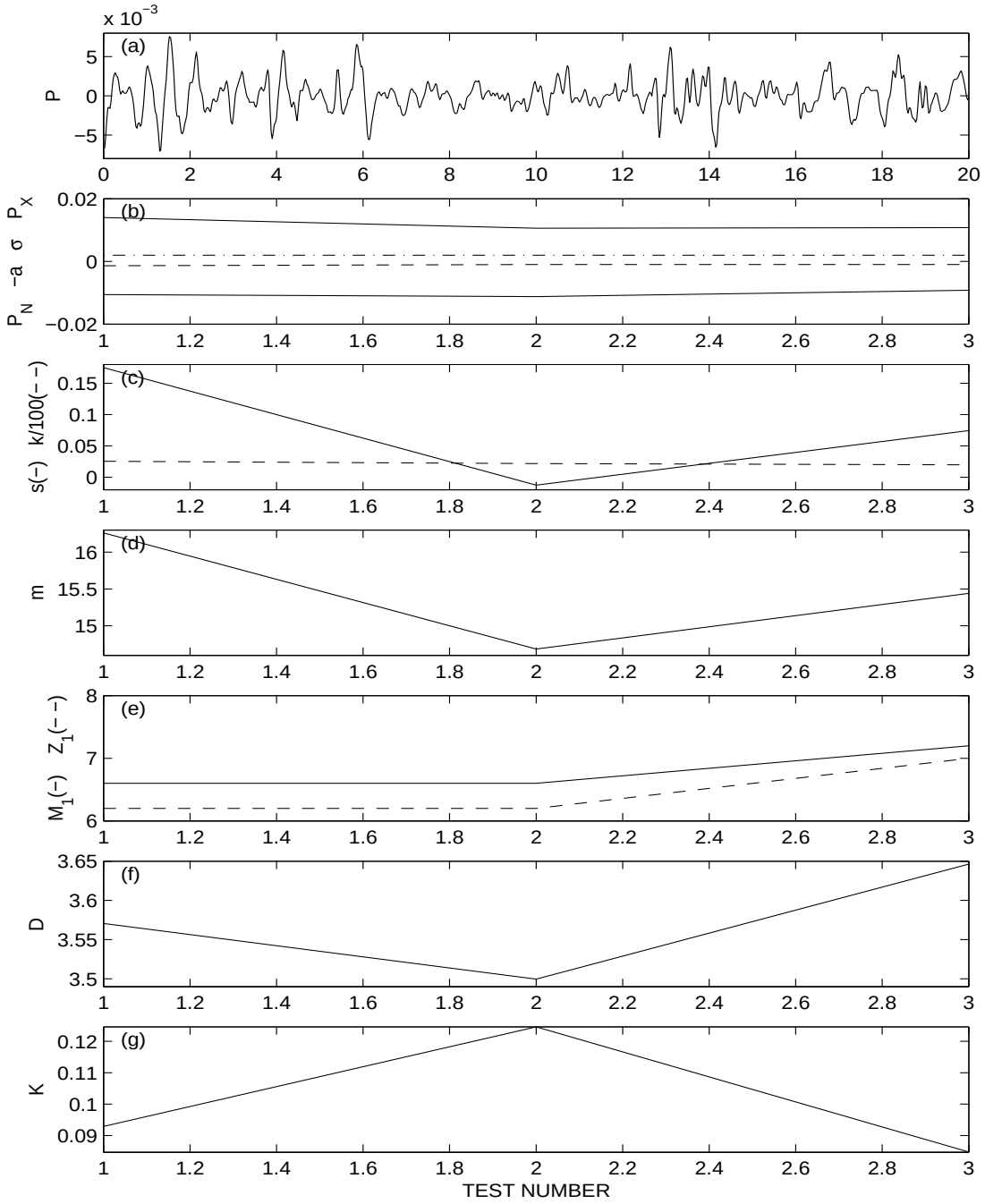

Figure 1: Results for EPRI air-gap offset seeded fault: (a) vibration power (*P*) versus time (milliseconds); (b) minimum (P_N), negative of the absolute average deviation (-*a*), standard deviation (σ), and maximum (P_X) of *P* for each test; (c) skewness (*s*) and kurtosis (*k*); (d) number of time steps per cycle (*m*); (e) first minimum in the mutual information function (M_1) and first zero in the autocorrelation (Z_1); (f) correlation dimension (*D*); and (g) Kolmogorov entropy (*K*).

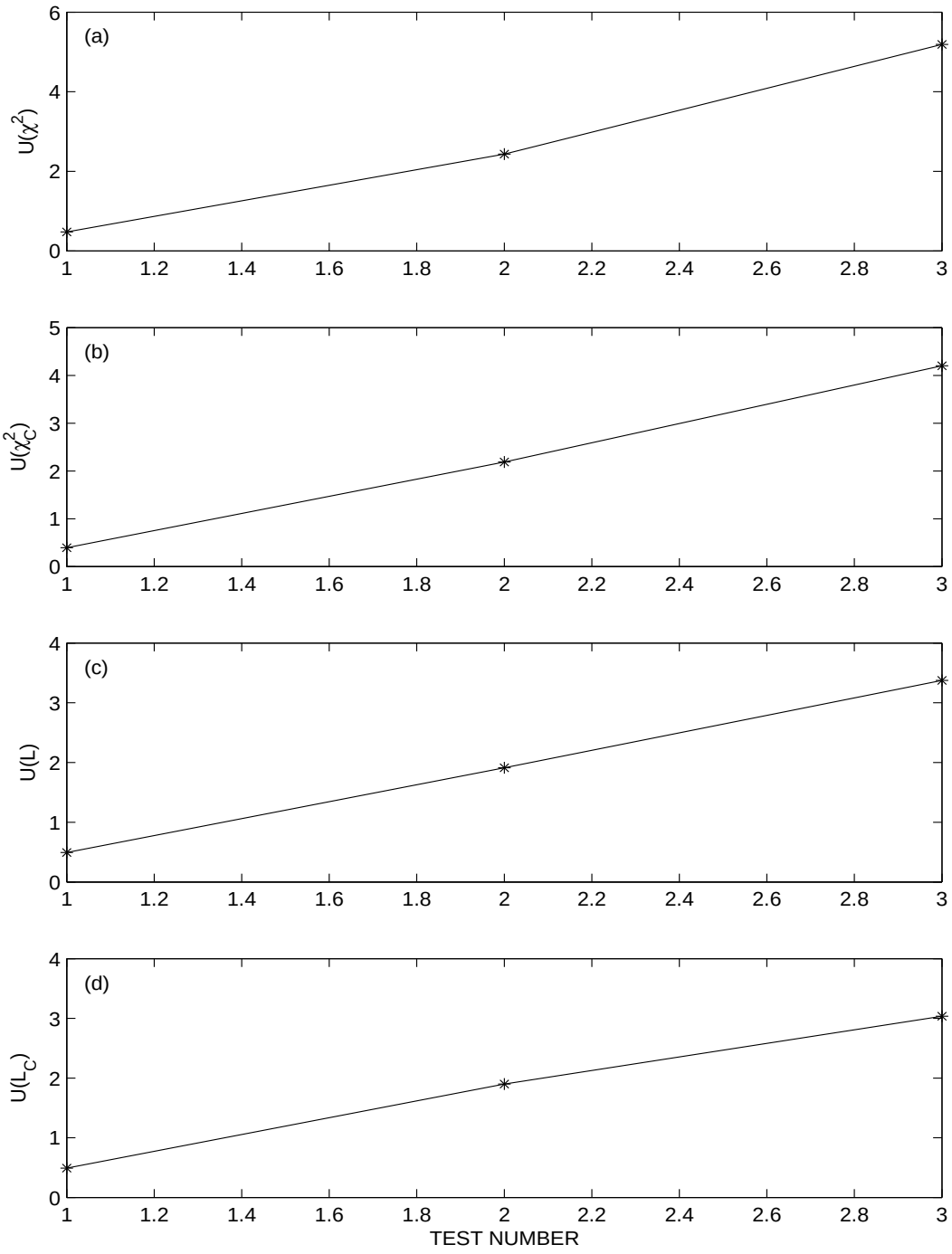

Figure 2: Plots of the four nonlinear dissimilarity measures for the airgap-offset seeded-fault from vibration power with the following phase-space parameters: d=3, S=3, λ=11. Dataset #1 is for the nominal (no fault) state. Datasets #2-3 are for two different airgap-offset faults.

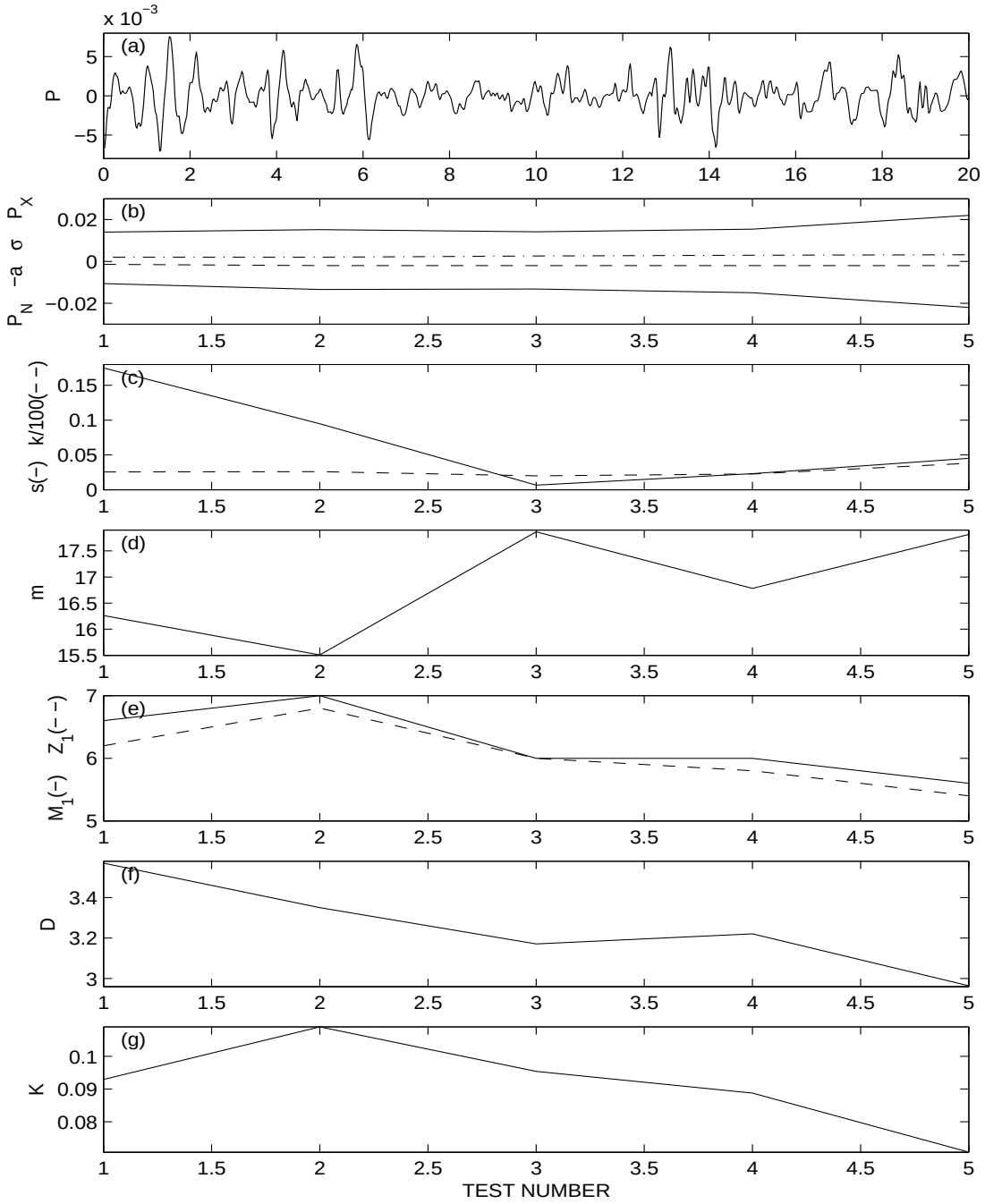

Figure 3: Results for EPRI broken-rotor seeded fault: (a) vibration power (*P*) versus time (milliseconds); (b) minimum (P_N), negative of the absolute average deviation (-*a*), standard deviation (σ), and maximum (P_X) of *P* for each test; (c) skewness (*s*) and kurtosis (*k*); (d) number of time steps per cycle (*m*); (e) first minimum in the mutual information function (M_1) and first zero in the autocorrelation (Z_1); (f) correlation dimension (*D*); and (g) Kolmogorov entropy (*K*).

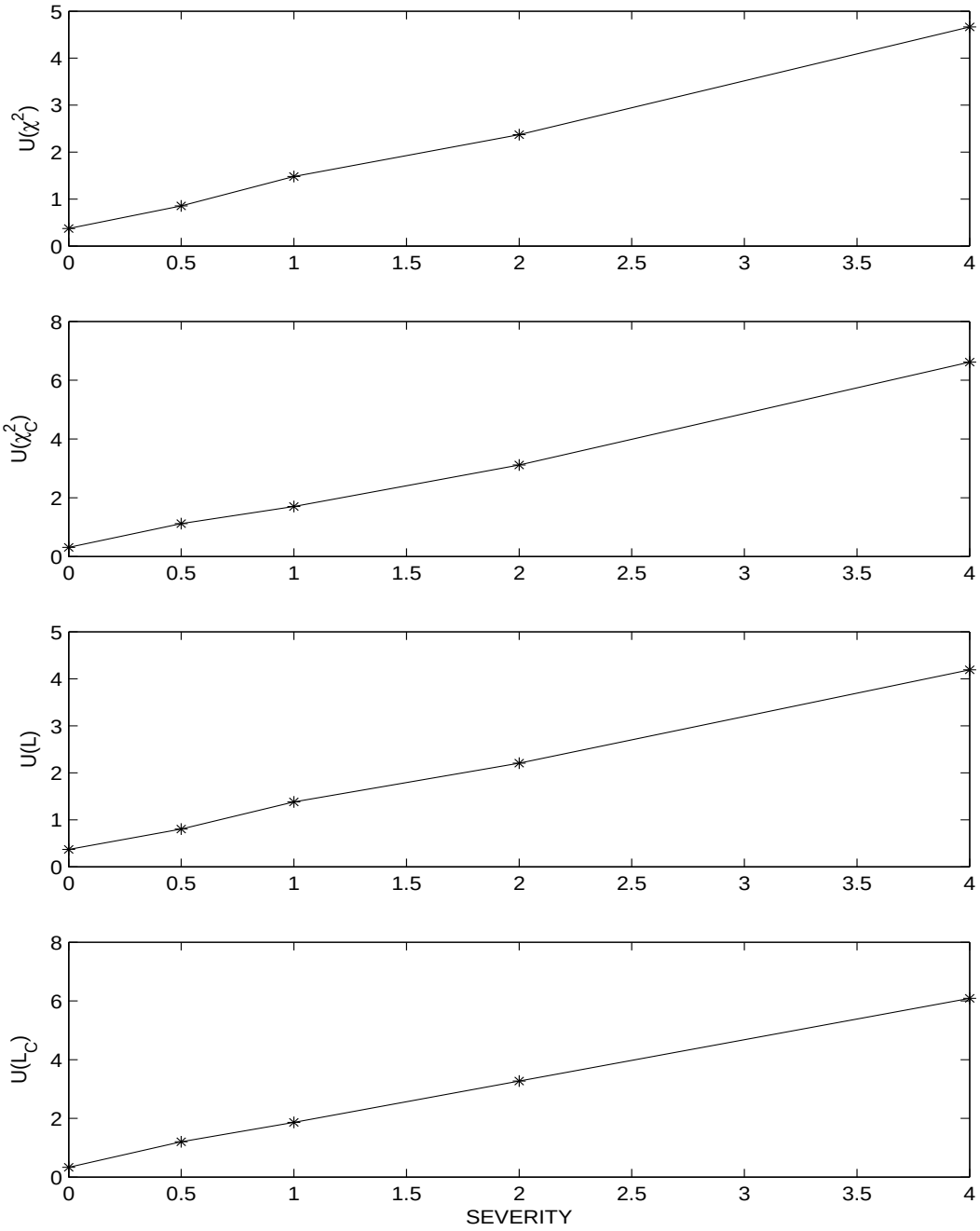

Figure 4: Plots of the four nonlinear dissimilarity measures for the broken-rotor seeded-fault vibration power data versus fault severity (number of broken rotor bars). Dataset #1 is for the nominal (no fault) state. Dataset #2 is for the 50% cut in one rotor bar. Dataset #3 is for the 100% cut in one rotor bar. Dataset #4 is for two cut rotor bars. Dataset #5 is for four cut rotor bars. The PS reconstruction parameters are: d=3, S=130, and λ=21.

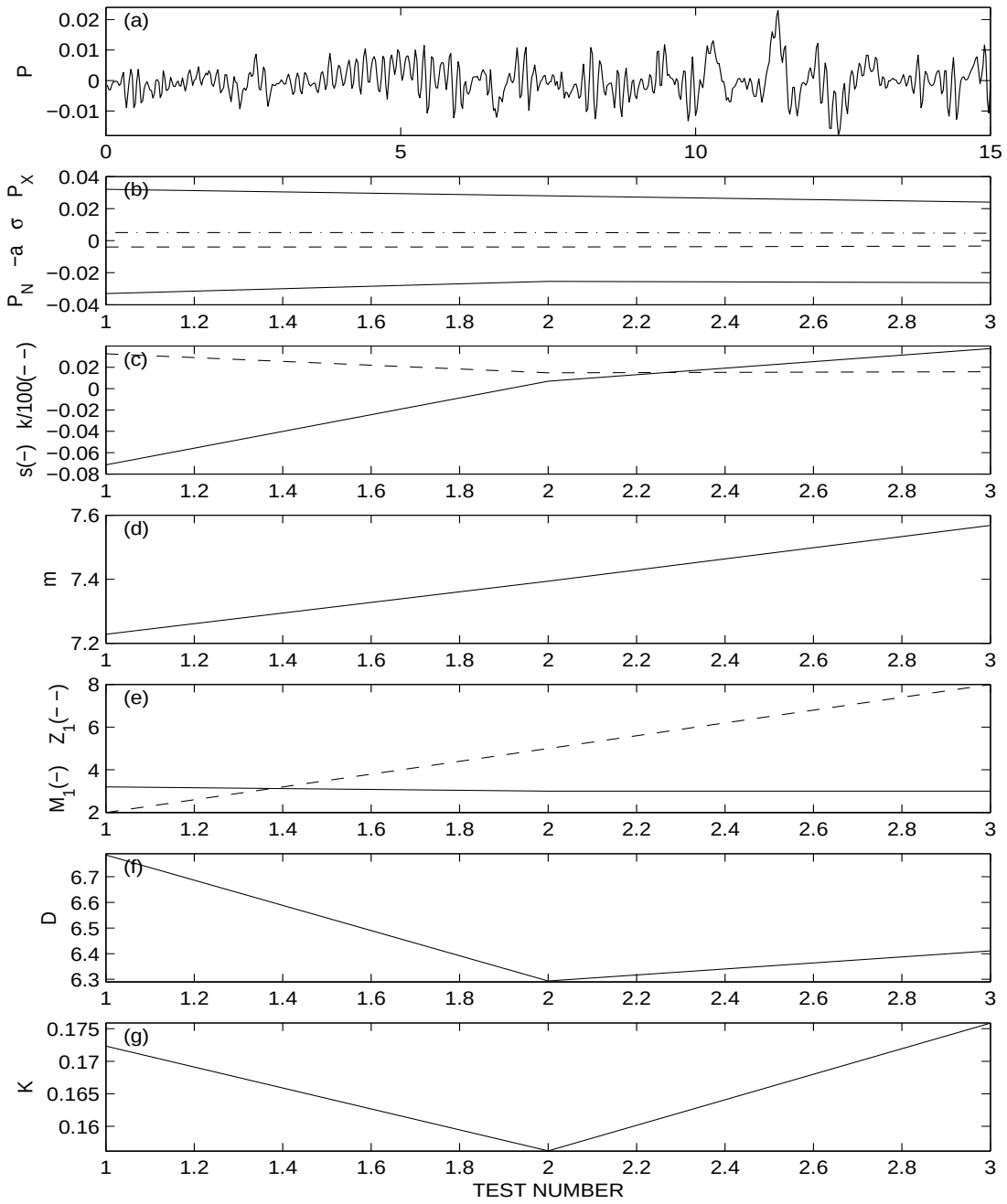

Figure 5: Results for EPRI turn-to-turn seeded fault: (a) vibration power (P) versus time (milliseconds); (b) minimum (P_N), negative of the absolute average deviation ($-a$), standard deviation (σ), and maximum (P_X) of P for each test; (c) skewness (s) and kurtosis (k); (d) number of time steps per cycle (m); (e) first minimum in the mutual information function (M_1) and first zero in the autocorrelation (Z_1); (f) correlation dimension (D); and (g) Kolmogorov entropy (K).

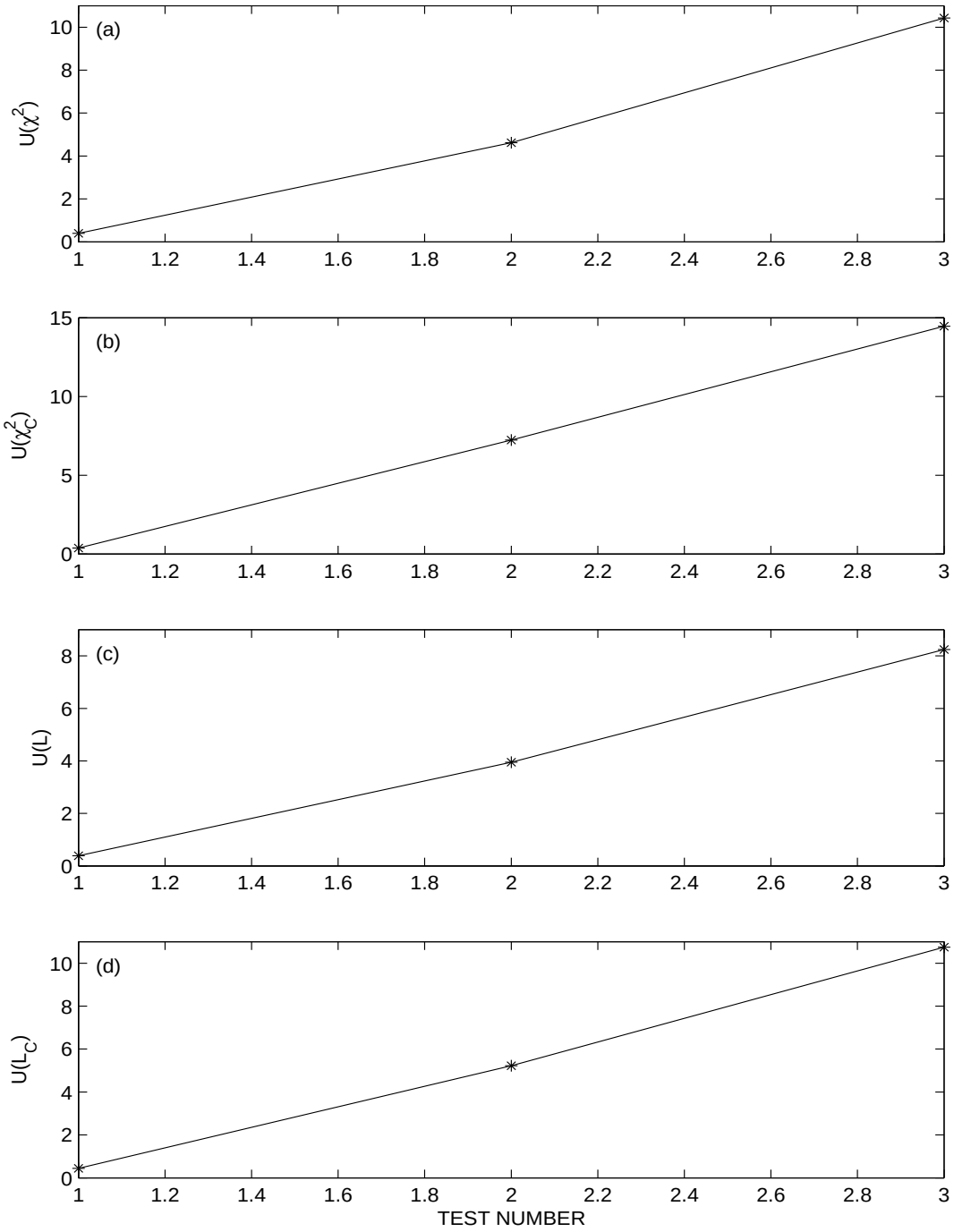

Figure 6: Plots of the four nonlinear dissimilarity measures from the turn-to-turn short seeded-fault vibration power. Dataset #1 is for the nominal (no fault) state. Dataset #2 is for the 2.7-ohm short. Dataset #3 is for the 1.35-ohm short. The PS reconstruction parameters are: d=2, S=6, λ=57.

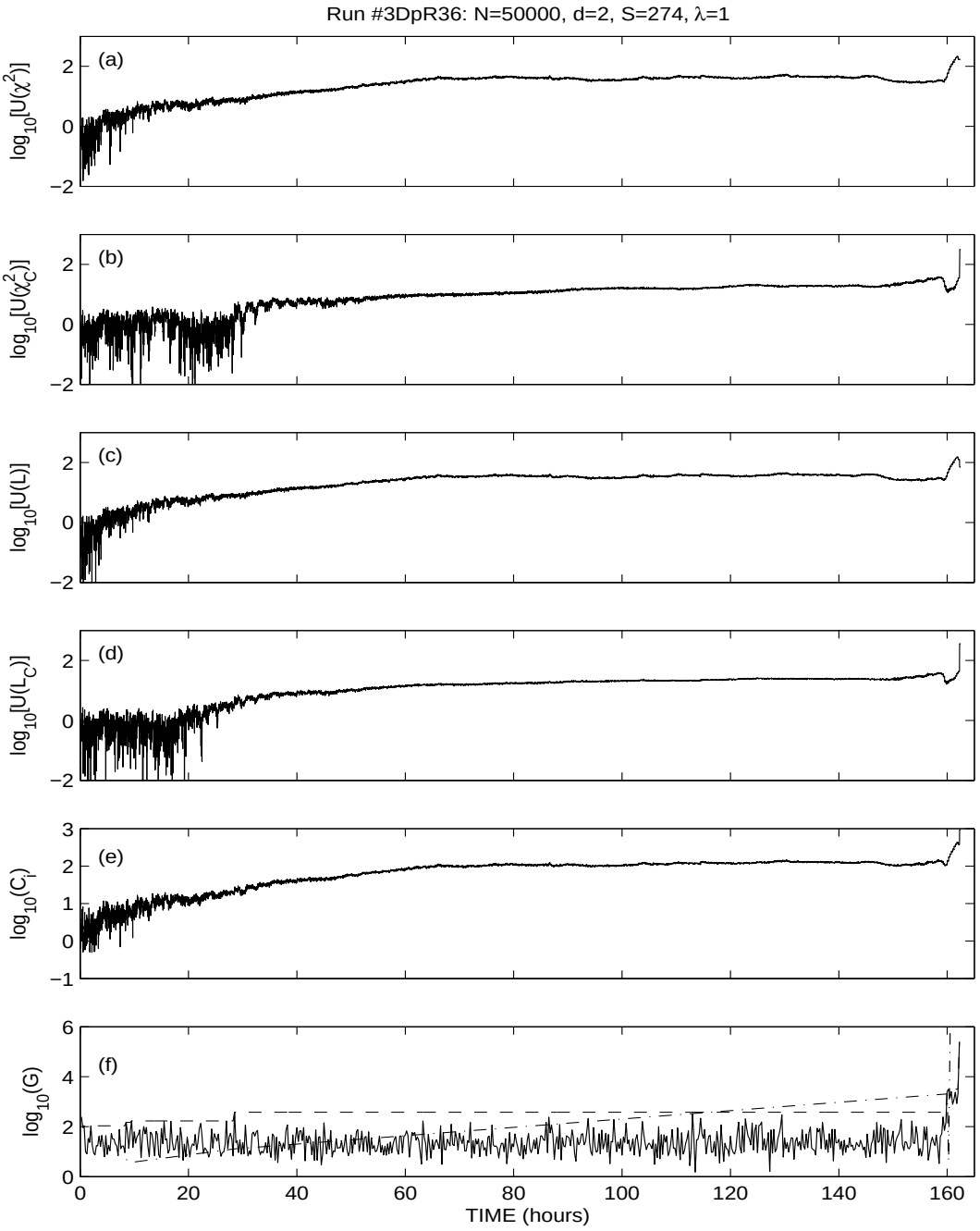

Figure 7: Phase-space dissimilarity measures versus time for the MDTB accelerated failure test (Run #36) from vibration power data: (a) – (d) the four renormalized PSDM; (e) composite measure, C_i, of the four PSDM; (f) end-of-life indicator, G (solid), running maximum of G (dashed), and ratio, r, of successive maxima (-.-) in G. Note that the vertical axis is the $\log_{10}$ of the parameter in subplots (a)-(f), and that $3\log_{10}(r)$ is plotted in (f) for clarity. The phase-space parameters are S=274, d=2, and λ=1, which are identical to those used in previous analysis[32] to show forewarning consistency.

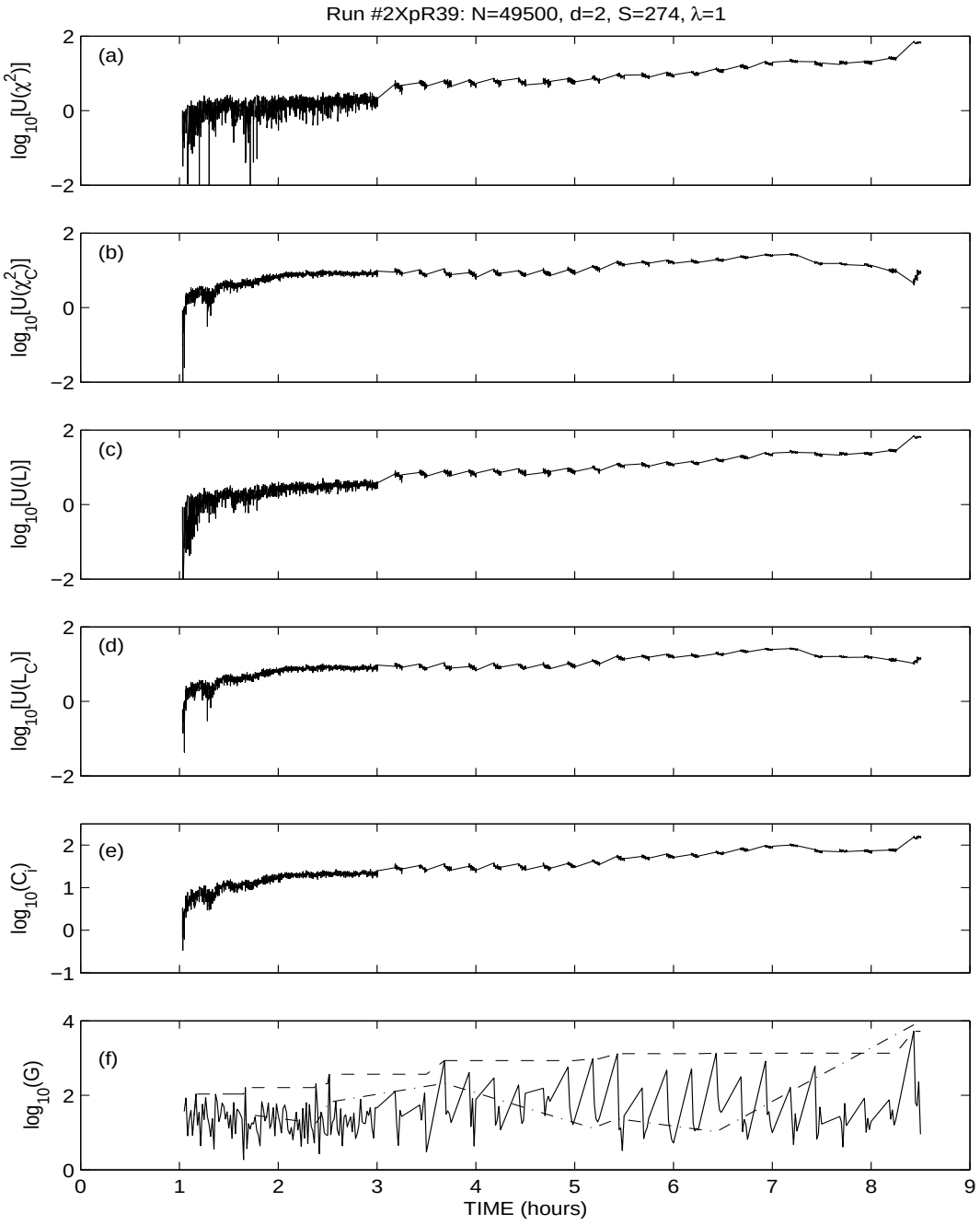

Figure 8: Phase-space dissimilarity measures versus time for the MDTB accelerated failure test (Run #39 2X portion) from vibration power data: (a) – (d) the four renormalized PSDM; (e) composite measure, C_i, of the four PSDM; (f) end-of-life indicator, G (solid), running maximum of G (dashed), and ratio, r, of successive maxima (-.-) in G. Note that the vertical axis is the $\log_{10}$ of the parameter in subplots (a)-(f), and that $3\log_{10}(r)$ is plotted in (f) for clarity. The phase-space parameters are S=274, d=2, and λ=1, which are identical to those used in previous analysis[32] to show self-consistency.

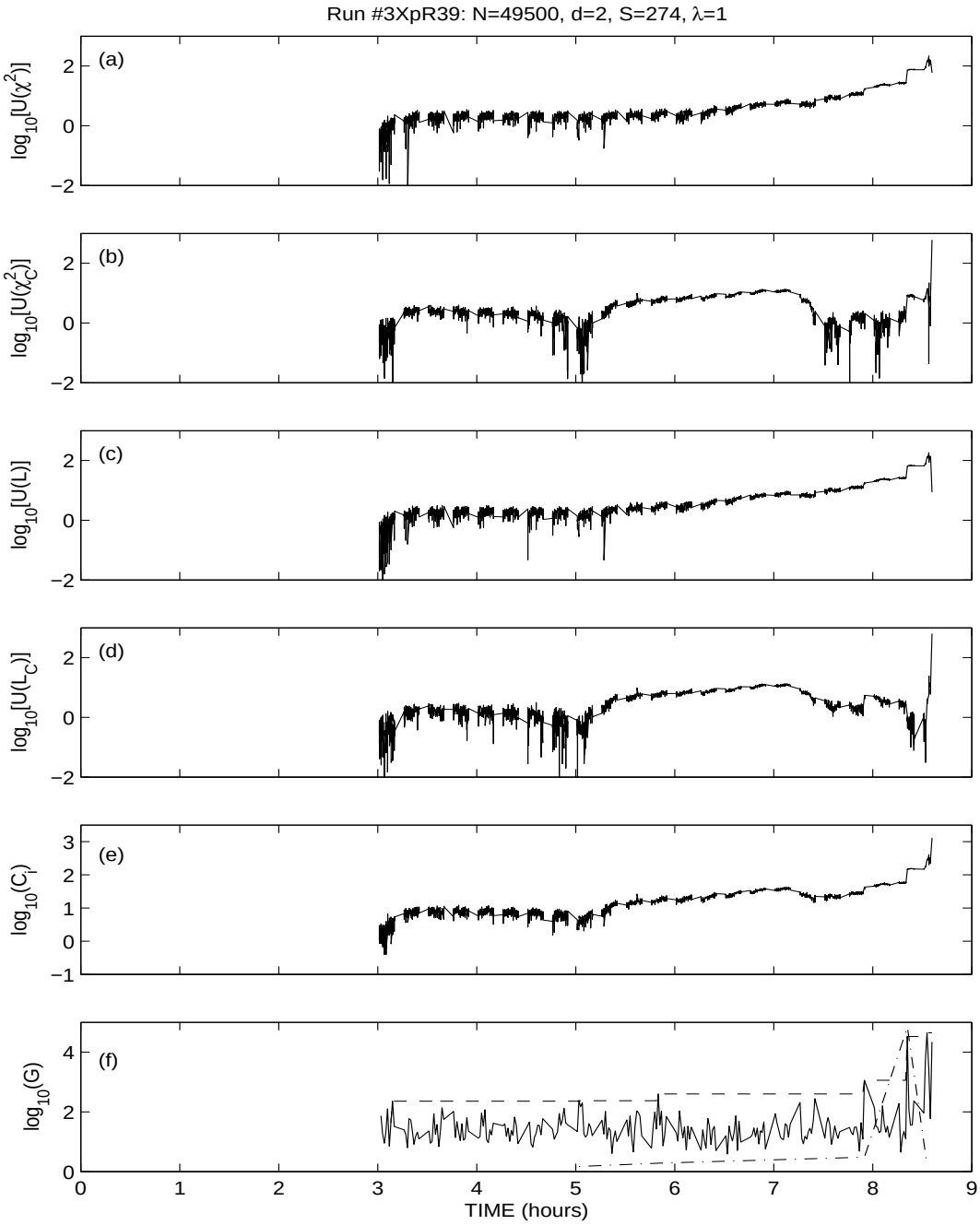

Figure 9: Phase-space dissimilarity measures versus time for the MDTB accelerated failure test (Run #39 3X portion) from vibration power data: (a) – (d) the four renormalized PSDM; (e) composite measure, C_i, of the four PSDM; (f) end-of-life indicator, G (solid), running maximum of G (dashed), and ratio, r, of successive maxima (-.-) in G. Note that the vertical axis is the $\log_{10}$ of the parameter in subplots (a)-(f), and that $3\log_{10}(r)$ is plotted in (f) for clarity. The phase-space parameters are S=274, d=2, and λ=1, which are identical to those used in previous analysis[32] to show self-consistency.

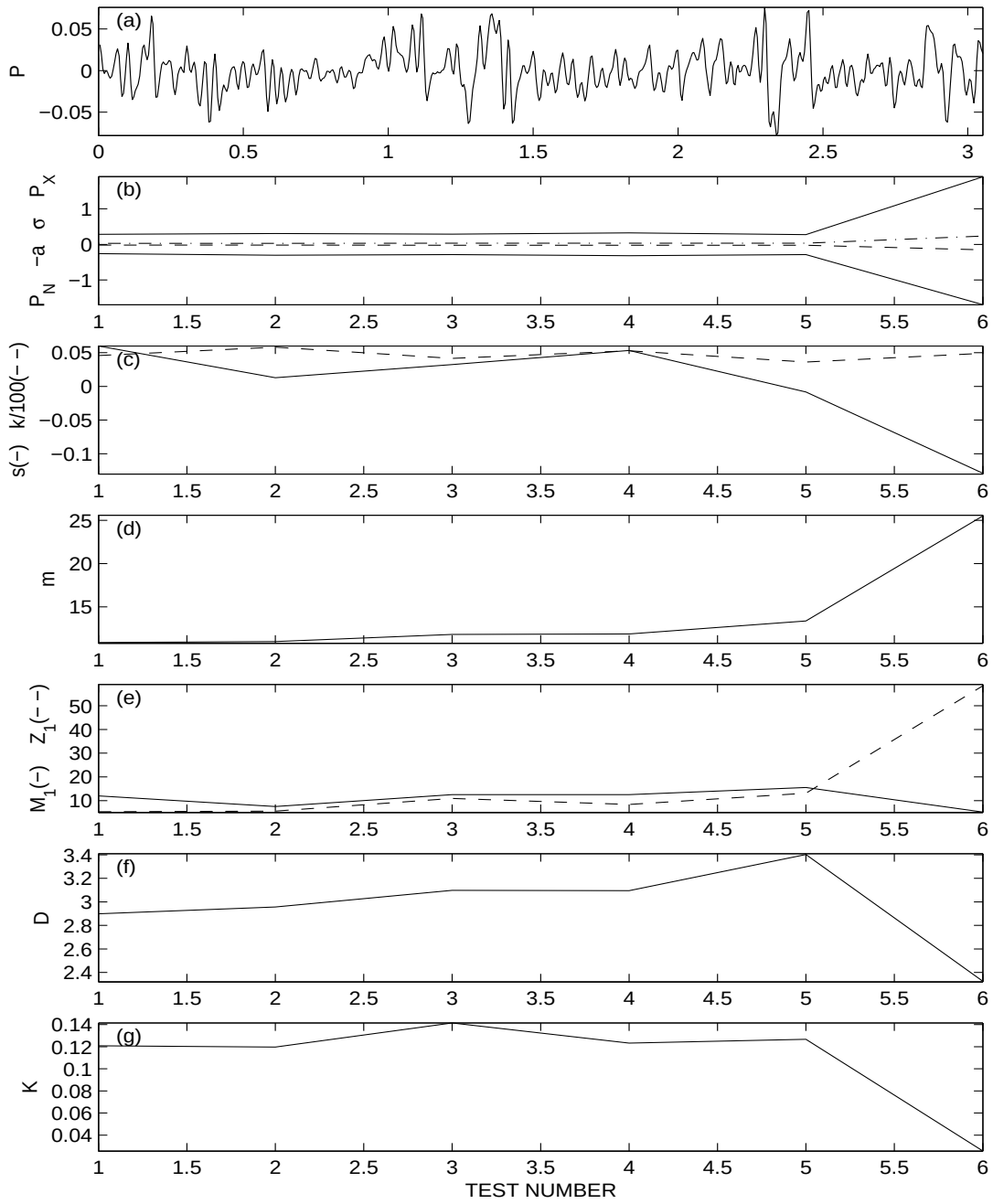

Figure 10: Results for PSU seeded shaft-crack fault: (a) vibration power (*P*) versus time (milliseconds); (b) minimum (P_N), negative of the absolute average deviation (-*a*), standard deviation (σ), and maximum (P_X) of *P* for each test; (c) skewness (*s*) and kurtosis (*k*); (d) number of time steps per cycle (*m*); (e) first minimum in the mutual information function (M_1) and first zero in the autocorrelation (Z_1); (f) correlation dimension (*D*); and (g) Kolmogorov entropy (*K*).

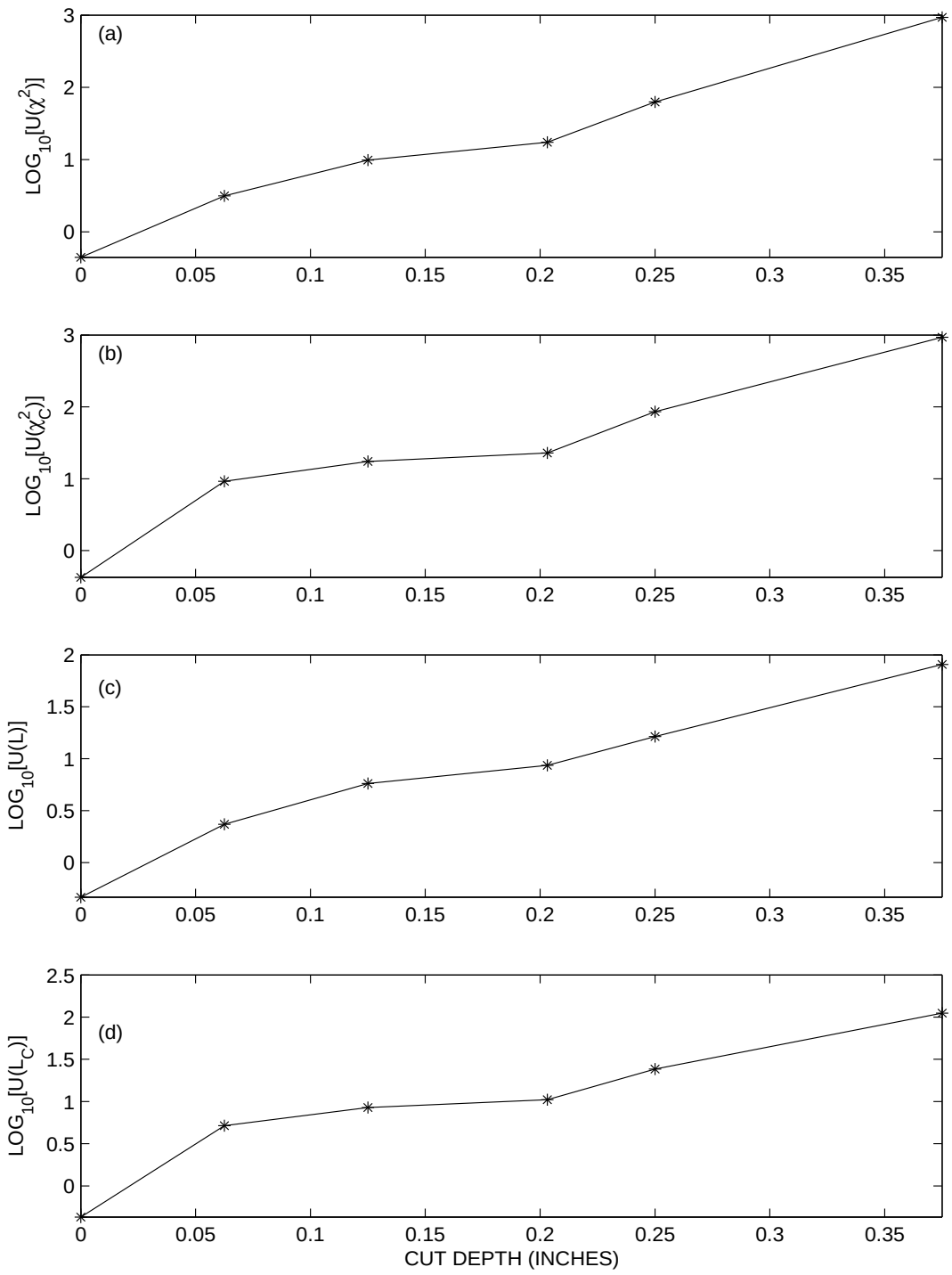

Figure 11: The four PSDM versus cut depth for the shaft-crack seeded-fault from vibration power data. This result is for the best set of phase-space parameters: S=2, d=4, λ=23, B=10, and N=100,000.

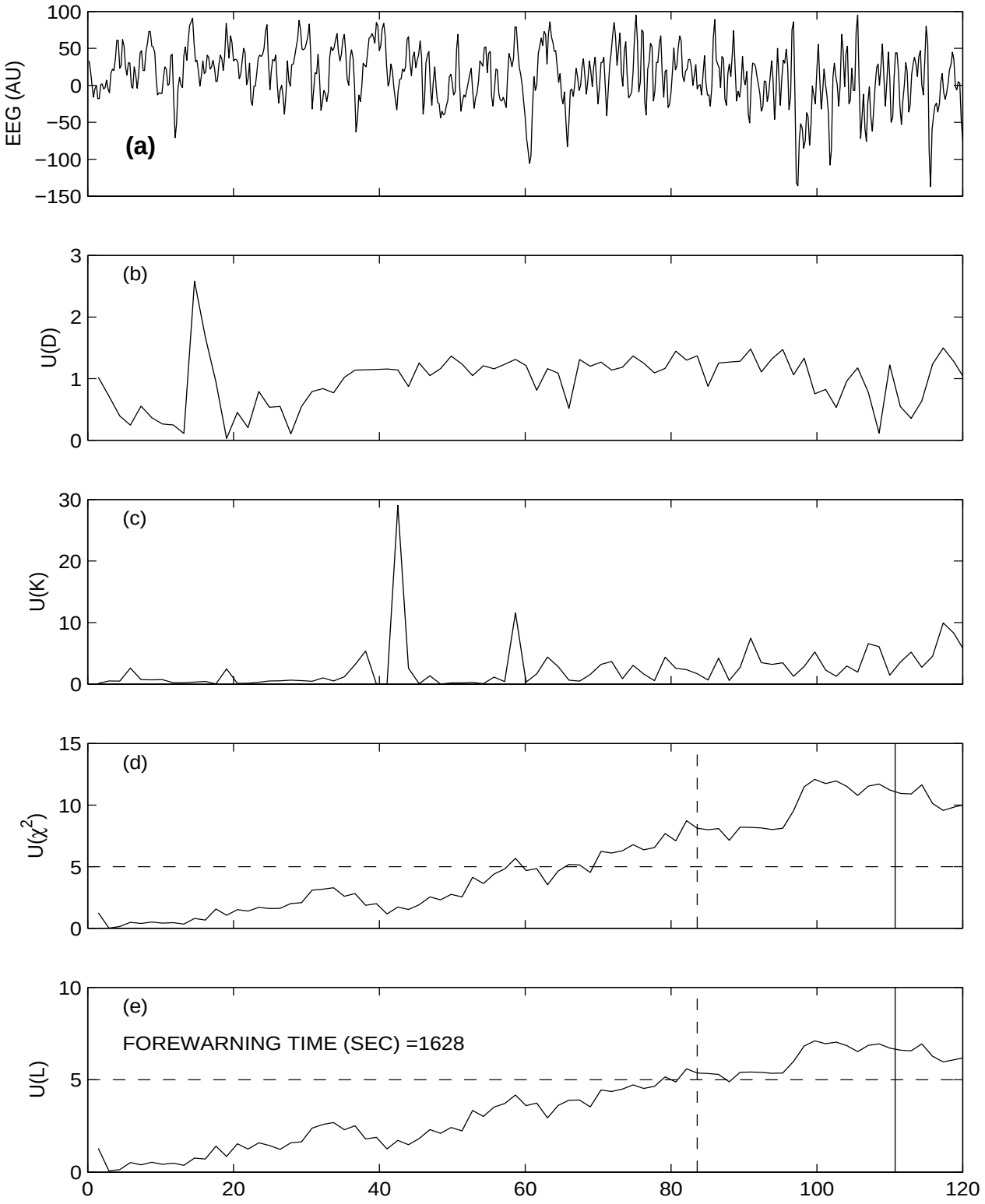

Figure 12: Results for human electroencephalogram channel 5 of dataset #PVM006, showing time-serial plots for: (a) 2.4 seconds of raw data collected at 250Hz, (b) correlation dimension, *D*, (c) Kolmogorov entropy, *K*, (d) $U(\chi^2)$, and (e) $U(L)$. The phase-space dissimilarity measures in subplots (d) and (e) are for $d = 3$, $S = 20$, $\lambda = 17$, and after removal of eye blink artifacts. Each cutest has $N = 22{,}000$ points, corresponding to 88 seconds. We have successfully applied this analysis to over sixty human datasets

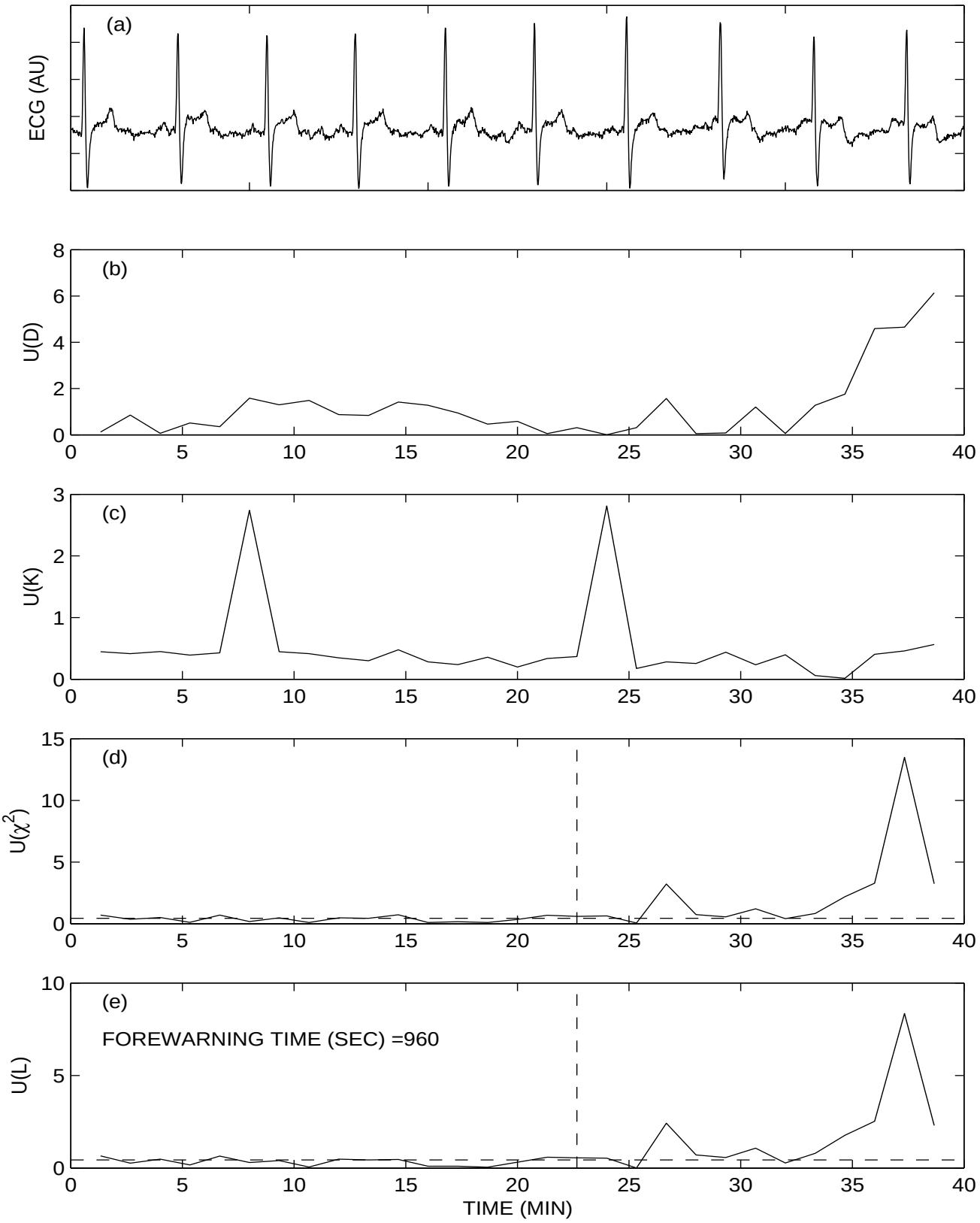

Figure 13: Results for human dataset #EC8202, showing time-serial plots for: (a) 10 seconds of raw heart wave data collected at 250 Hz, (b) correlation dimension, D, (c) Kolmogorov entropy, K, (d) $U(\chi^2)$, and (e) $U(L)$. The phase-space dissimilarity measures in subplots (d) and (e) are for d= 5, S = 3, λ = 27, after removal of breathing artifacts. Each cutest had N = 18,000 points, corresponding to 72 seconds.

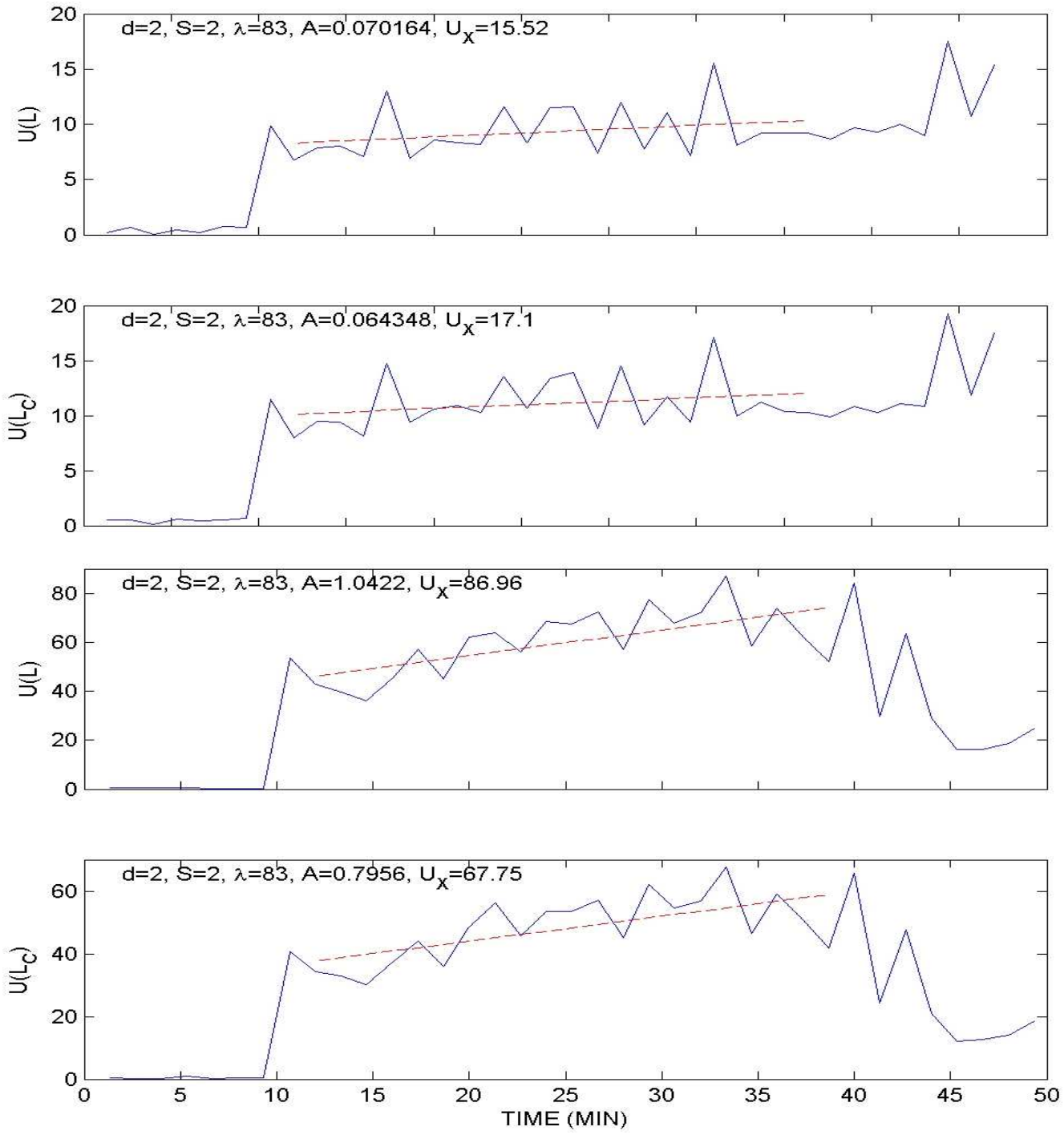

Figure 14: Results for human subject RAY show $U(L)$ and $U(L_C)$ when no syncope occurs (above the double line), in contrast with $U(L)$ and $U(L_C)$ when syncope does occur (below the double line). No results for traditional nonlinear measures are shown, due to their insensitivity in the other examples. The phase-space dissimilarity measures are for d =2, S = 2, λ = 83, after removal of breathing artifacts. Each cutest has N=20,000 points (80 seconds of data at a sampling rate of 250 Hz).

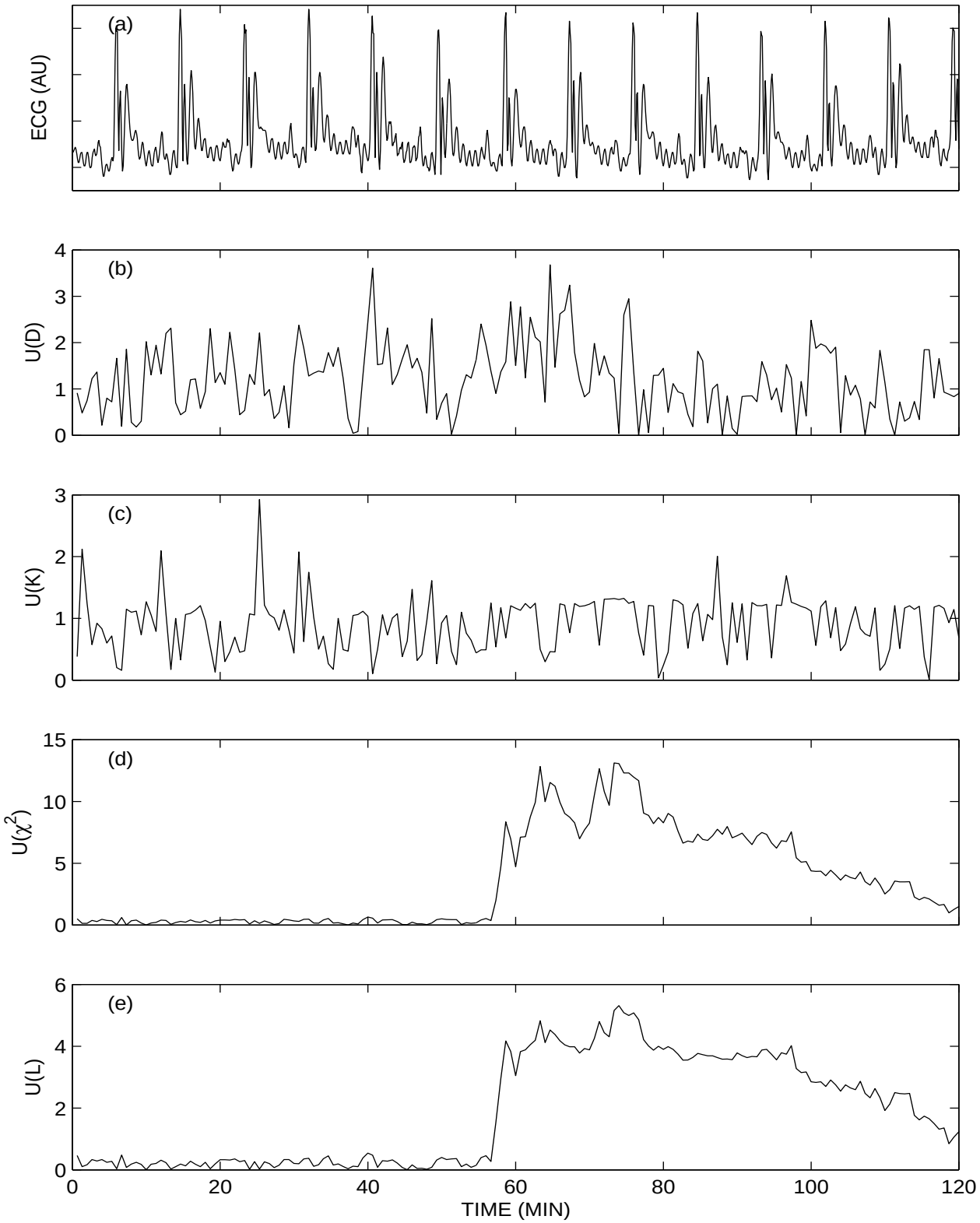

Figure 15: Results for dataset #33209V, showing time-serial plots for: (a) 2.4 seconds of raw rat heart wave data collected at 500 Hz, (b) correlation dimension, *D*, (c) Kolmogorov entropy *K*, *(d)* $U(\chi^2)$, and (e) $U(L)$. The phase-space dissimilarity measures in subplots (d) and (e) are for d =2, S = 2, λ = 80, after removal of breathing artifacts. Each cutest has N=20,000 points (40 seconds of data).

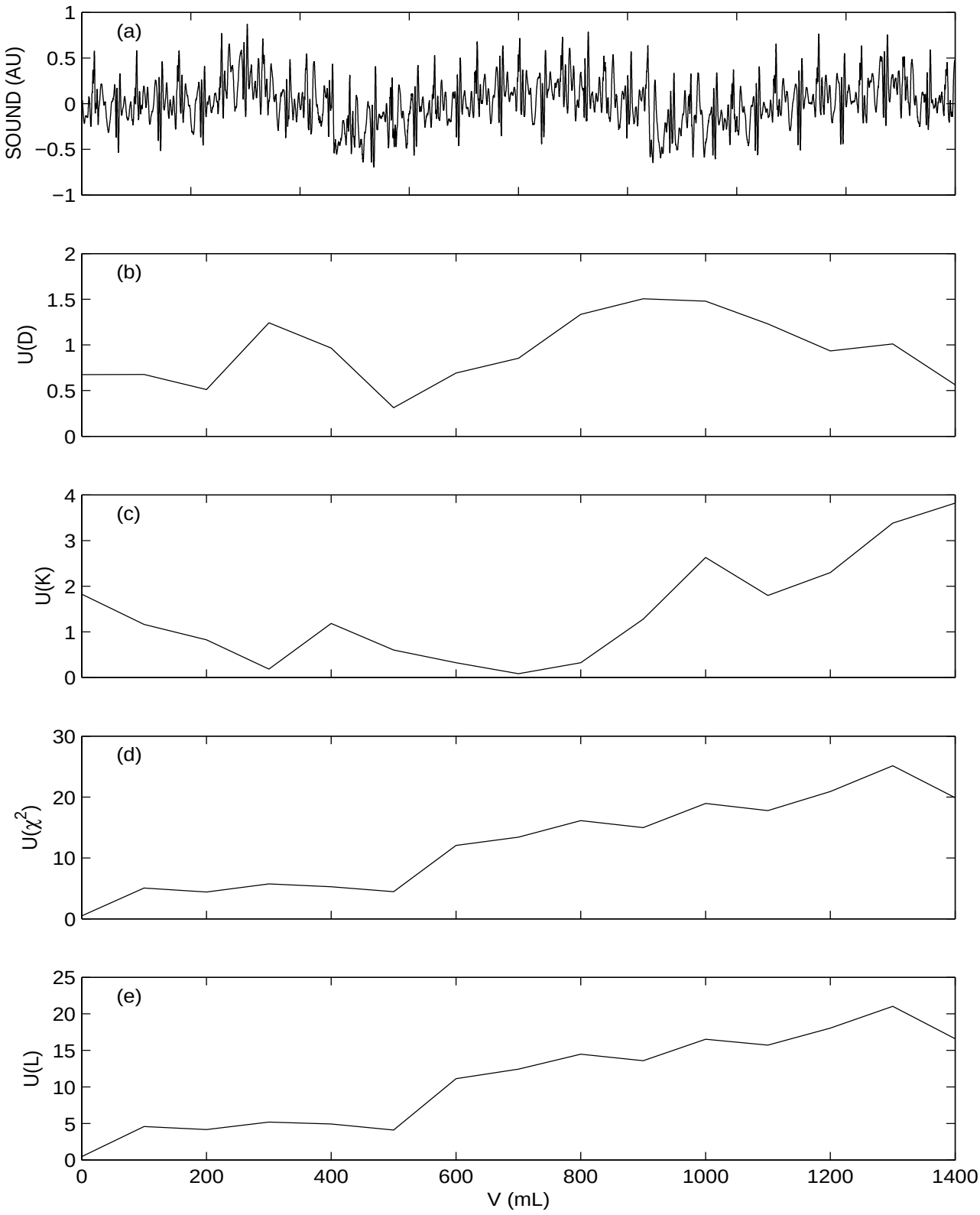

Figure 16: Results from dataset #PTX5, showing time-serial plots for: (a) 4 seconds of raw lung sounds data collected at 10 kHz, (b) correlation dimension, D, (c) Kolmogorov entropy, K, (d) $U(\chi^2)$, and (e) $U(L)$. The phase-space dissimilarity measures in subplots (d) and (e) are for d = 3, S = 30, λ = 20, after removal of breathing artifacts. Each cutest has N = 50,000 points (5 seconds of data).